ATTENUATION, SCATTER, AND SPATIAL RESOLUTION COMPENSATION IN SPECT

By

Michael A. King, Stephen J. Glick, P. Hendrik Pretorius, R. Glenn Wells, Howard C. Gifford, Manoj V. Narayanan, and Troy Farncombe

Division of Nuclear Medicine
Department of Radiology
The University of Massachusetts Medical School
55 Lake Ave North
Worcester, MA 01655

I. Review of the Sources of Degradation and Their Impact in SPECT Reconstruction

A. Ideal imaging

Data acquisition for the case of ideal SPECT imaging is illustrated in Figure 1, which portrays a single-headed gamma camera imaging a source distribution f(x,y) at a rotation angle θ with respect to the x-axis. The camera is equipped with a parallel-hole absorptive collimator, which for this ideal case only allows photons emitted from f(x,y) in a direction parallel to the collimator septa to pass through to the NaI(Tl) crystal, and be detected. The source distribution in Figure 1 is a cartoon drawing of a slice through the three-dimensional (3D) mathematical cardiac-torso (MCAT) phantom [1] with a Tc-99m sestamibi distribution. Let (t, s) be a coordinate system rotated by the angle θ counter-clockwise with

respect to the (x, y) coordinate system. Then t and s can be written in terms of x and y, and the rotation angle θ as [2]:

$$t = x \cos \theta + y \sin \theta \qquad (1)$$
$$s = -x \sin \theta + y \cos \theta .$$

The ray sum ($p(\theta,t')$) is the line integral over f(t,s) with respect to s for t = t', or

$$p(\theta, t') = \int_{-\infty}^{\infty} f_\theta(t',s)\, ds = \int_{-\infty}^{\infty} \int_{-\infty}^{\infty} f_\theta(t,s)\, \delta(t-t')\, dt\, ds = \int_{-\infty}^{\infty} \int_{-\infty}^{\infty} f(x,y)\, \delta(x\cos\theta + y\sin\theta - t')\, dx\, dy , \quad (2)$$

where δ is the delta function, and Equation 1 was used to express t in terms of x, y, and θ. The function $p(\theta,t)$ for the case of ideal imaging is the Radon transform of f(x,y), and is the parallel projection of f(x,y) for a constant value of θ [3]. By rotating the camera head about the patient a set of projections is acquired for different projection angles. This set of projections constitutes the data that will be used to estimate the source distribution from which they originated. Figure 2 shows the overlaid ideal projections of a point source in the liver of the MCAT phantom at projection angles of 0^0 (left lateral), 45^0 (left-anterior oblique), 90^0 (anterior), and 135^0 (right-anterior oblique) relative to the x-axis in Figure 1. The location of the point source is indicated as the black circular point within the liver and on the x-axis in Figure 1. Notice in the ideal case, the projections are all of the same size and shape, and vary with projection angle just in their positioning along the t-axis. When the projections are stacked one on top of the other for viewing, they form a matrix called the sinogram. The matrix is so named because with 360 degree acquisitions each location traces out a sine function whose amplitude depends on the distance from the center-of-rotation (COR) and phase depends on its angular location.

B. Sources of image degradation

SPECT imaging is not ideal, however. Inherent in SPECT imaging are degradations, which distort the projection data. This chapter will focus on three such degradations, and the compensation for them. The first is attenuation. In order for a photon to become part of a projection, it must escape the body. As illustrated in Figure 3, photons emitted such that they would otherwise be detected may be either photoelectrically absorbed (photon A) or scattered (photon B) such that they will be lost from inclusion in the projections. Thus the attenuated projections ($p_A(\theta,t)$) will contain fewer events than the ideal projections. This is illustrated in Figure 4, which shows the attenuated projections of the point source of Figure 2. Note how the reduction in the number of detected events varies with the thickness and nature of material through which the photons must travel to be imaged. The extent of attenuation can be quantified mathematically by the transmitted fraction (TF(t', s', θ)), which is the fraction of the photons from location (t', s') that will be transmitted through a potentially non-uniform attenuator at angle θ. The transmitted fraction is given by:

$$TF(t', s', \theta) = \exp\left(-\int_{s'}^{\infty} \mu(t',s)\, ds\right) , \qquad (3)$$

where μ(t,s) is the distribution of linear attenuation coefficients as a function of location. Equation 3 is accurate only for a mono-energetic photon beam, and under the assumption that as soon as a photon undergoes any interaction, it is no longer counted as a member of the beam. The latter is the "good geometry" condition [4,5]. The attenuated projections are obtained from the ideal projections by including TF within the integrals of Equation 2. As a result of the differences in attenuation coefficient with type of tissue, the TF will vary with the materials traversed even if the total patient thickness between the site of emission and the camera is the same. That is, it makes a difference if the photons are passing through muscle, lung, or bone. Similarly, a change in TF will occur if the amount of tissue that has to be traversed is altered. Thus, one needs to have patient-specific information on the spatial distribution of attenuation coefficients (an attenuation map or estimate of μ(t,s)) in order to calculate the attenuation that occurs when photons are emitted from a given location in the patient and detected at a given angle.

   The second source of degradation, which will be considered in this chapter, is the inclusion of scatter in the projections. This, as is illustrated in Figure 5, leads to the inclusion of photons in the projections that normally would not have been detected. Note that in Figure 6 a logarithmic scaling is used for the number of counts detected to better illustrate the contribution of scatter. To account for the presence of scatter, Equation 3 can be modified by multiplying the exponential term by a buildup factor (B) [4]. The buildup factor is the ratio of the total number of counts detected within the energy window (primary plus scatter) to the number of primary counts detected within the window. In the "good geometry" case there is no scatter detected, so the buildup factor is 1.0. For the four point-source projections in Figure 6 the buildup factors were 1.40 for the RAO view, 1.52 for the anterior view, 1.84 for the left-anterior oblique view, and 2.21 for the left lateral view. Photons undergoing classical scattering do not change energy during the interaction; thus they can not be separated from transmitted photons on the basis of their energy. At the photon energies of interest in SPECT imaging, classical scattering only makes up a small percentage of the interactions in the human body. Compton scattering is the dominant mode of interaction under these conditions, and during Compton scattering the photon is reduced in energy as well as deflected from its original path. Thus one can use energy windowing to reduce the amount of scattered photons imaged, but not eliminate scatter, due to the presence of classically scattered photons and the finite energy resolution of current imaging systems. In fact, the ratio of scattered to primary photons in the photopeak energy window (scatter fraction) is typically 0.34 for Tc-99m [6] and 0.95 for Tl-201 [7]. When scatter is neither removed from the emission profiles prior to reconstruction nor incorporated into the reconstruction process, it can lead to over-correction for attenuation because the detected scattered photons violate the "good geometry" assumption of Equation 3.

   The third source of degradation is the finite, distance-dependent spatial resolution of the imaging system. When imaging in air, the system spatial resolution consists of two independent sources of blurring [5]. The first is the intrinsic resolution of the detector and electronics, which is well modeled as a Gaussian function. The second is the spatially varying geometrical acceptance of the photons through the holes of the collimator. This response is illustrated in Figure 7. Note in this figure that both photon A, which is emitted parallel to the s-axis, and photon B, which is angled relative to the s-axis, now make it through the collimator and are detected. Detailed theoretical analyses of the geometrical point-spread and transfer functions for multihole collimators have been published [8-11]. In the absence of septal penetration and scatter, the point-spread function (PSF) for parallel-hole collimators is typically approximated as a Gaussian function [12-13] whose standard deviation (σ_C) is a linear function of distance given as:

$$\sigma_C (d) = \sigma_0 + \sigma_d \bullet d , \tag{4}$$

where d is distance from the face of the collimator, σ_0 is the standard deviation at the face of the collimator, and σ_d is the change in standard deviation with distance. Since the two sources of blurring are independent, they can be analyzed as sub-systems in series [14]. Therefore, the system PSF is the convolution of the collimator and intrinsic PSF's. The convolution of two Gaussian functions is a third Gaussian function. Thus, the system PSF can be approximated by a Gaussian function whose distance-dependent standard deviation (σ_S) is given as:

$$\sigma_S\,(d) = (\sigma_C^2\,(d) + \sigma_I^2)^{1/2}\,, \tag{5}$$

where σ_I is the standard deviation of the Gaussian function modeling the intrinsic spatial resolution. Illustration of the system PSF's for the point source in the liver of the MCAT phantom is given in Figure 8 for the same 4 projection angles employed in the previous figures. Note the variation in the heights and widths of these responses due to the variation in distance between the point source and the face of the collimator.

Attenuation, scatter, and system spatial resolution are three important physical sources of image degradation in SPECT when imaging with Tc-99m or Tl-201, but they are not the only ones. Other sources include collimator scatter and x-ray production, septal penetration, patient and physiological motion, and non-static tracer distributions. The extent to which each of these is important varies with the energy of the photons emitted, the kinetics of the radiopharmaceutical, and the time required for imaging the patient. A full discussion of all these factors is beyond the scope of this chapter.

C. Impact of degradations

As detailed in a previous chapter, filtered backprojection (FBP) provides an exact, analytical solution to reconstructing a slice from the projections in the sinogram. That is, FBP provides an inversion of the Radon transform [3]. However, as should now be clear, inverting the Radon transform is only part of the problem. Attenuation of the photons, the acquisition of scattered as well as transmitted photons, and the inherent distance-dependent finite resolution of the imaging system have also distorted the acquired projections from the ideal projections. The result is that just inverting the Radon transform does not result in an accurate estimate of the original source distribution, even in the absence of noise. This is illustrated in Figure 9. Figure 9A shows the source distribution used to create the projections. Figure 9B shows the slice reconstructed using FBP from ideal projections. Notice that an extremely good estimate of the original source distribution is obtained. Figure 9C shows the FBP reconstruction of the slice from projections that have been degraded by the presence of attenuation, scatter, and system spatial resolution. Notice the significant distortion in the intensities and shapes of the structures when the sources of degradation are included in creating the projections, but are not included in the reconstruction process. For example, due to attenuation and the partial-volume effect (as detailed in section IV), the heart wall is significantly reduced in apparent intensity compared to the soft tissues. Also, the soft tissue close to the body surface is now enhanced compared to that of the deeper tissues. Finally, note the significant distortion of the areas of low activity concentration around the heart and liver, and the buildup of counts outside the body in the sternal notch region on the anterior surface. The goal of the compensation strategies discussed in this chapter is to return the slice estimate of Figure 9C to that of Figure 9A; however, the compensation strategies are limited in their ability to perform such a transformation by the presence of noise. The complication of the presence of noise is illustrated in Figure 9D, which shows the

FBP reconstruction of the degraded projections to which has been added Poisson noise typical of that in perfusion imaging.

The cause of the distortions in Figure 9C is the inconsistency of the projection data with the model of imaging used in reconstruction. The model of the imaging system used with FBP reconstruction was that of an ideal imaging system (i.e., one with a PSF equal to a δ-function whose integral is a constant independent of projection angle, as illustrated in Figure 2). The actual PSF's for SPECT imaging vary in shape and magnitude with location in the slice and projection angle, as illustrated in Figure 8. Without compensation for such variation prior to reconstruction, or accounting for the variation as part of the reconstruction algorithm, the reconstructed PSF is anisotropic with long positive and negative tails [15]. The reason for this is as follows. Use of the "ramp" filter in FBP to compensate for the blurring of backprojection results in negative values in the projections. These negative values cancel out the wrong guesses as to where the counts are located when backprojected. If the acquired PSF's are of different size and shape, then the cancellation is not exact, and a distorted reconstructed PSF results [16]. The low-magnitude tails of the reconstructed PSF's from hot structures in images can add up, causing changes in the apparent count level of nearby structures. Clinically, this can result in decreased apparent localization in the inferior wall of the heart in perfusion images with significant hepatic activity [17], the loss of the ability to visualize bone structures in bone scans at the level of significant bladder activity [18, 19], and other artifacts. The distortion is not limited to FBP, but occurs with iterative reconstruction if the imaging model is inconsistent with the actual data collection [16, 20].

II. Non-uniform Attenuation Compensation

A. Estimation of patient-specific attenuation maps

The determination of an accurate, patient-specific attenuation map is fundamental to performing attenuation compensation (AC). This fact has been appreciated for years [21]; however, it is the recent commercial interest in providing estimates of attenuation maps which will likely bring the benefits of AC into wide-spread clinical use. Three strategies have been employed for obtaining attenuation maps for use with AC: 1) import and register maps from another modality; 2) obtain transmission data for estimating the attenuation maps with the gamma camera employed for emission imaging; and 3) estimate the attenuation map from solely the emission data. A previous review of this topic can be consulted for more details than are presented in this chapter [22].

High-resolution images from another modality can be imported and registered with the patient's SPECT data [23, 24]. Of course the task is made a lot simpler by acquiring the high-resolution slices while the patient is on the same imaging table [25]. The voxel values in the high-resolution images require scaling to the appropriate attenuation coefficients for the energy of the emission photon [26]. Besides their use for attenuation maps, these images can also provide anatomical contexts for the emission distributions, and compensation for the partial-volume effect [27]. Currently one imaging company is marketing a combined SPECT and CT system that share a single imaging table. The image noise in the attenuation maps from such a system is very low, and the in plane resolution is very high compared to the SPECT slices. Such systems will most likely perform sequential emission and transmission imaging; however, the CT imaging time can be quite short if a high-end CT system is coupled with the SPECT system. One potential drawback to such a system is the cost, especially if it is desirable to use the CT system for diagnostic imaging as well as providing AC for the SPECT system.

The basic transmission source and camera collimator configurations are summarized in Figure 10 for a 50-cm field-of-view (FOV) single headed SPECT system imaging a 50-cm diameter patient. The extent of truncation illustrated would of course vary with the camera FOV and the patient diameter. With each of these configurations, the projections of the transmission source with the patient and table present in the FOV of the camera are combined with the transmission projections with the patient and table absent (blank scan) and input to reconstruction algorithms which solve Equation 3 for the µ's (attenuation map).

The first configuration, illustrated in Figure 10A, is that of a sheet transmission source opposite a parallel-hole collimator on the camera head. This configuration was investigated for a number of years for use with SPECT systems [28-30]. Its major advantage was that it provided a transmission source which fully irradiated the camera head opposed to it, and needed no motion of the source beyond that provided by the rotation of the gantry. The disadvantages of this configuration were that it was cumbersome to work with and required source collimation in order that "good geometry" attenuation coefficients were estimated [31].

The second configuration, which is shown in Figure 10B, is that of the multiple line-source array [32]. With this configuration, the transmission flux comes from a series of collimated line sources aligned parallel to the axis of rotation of the camera. The spacing and activity of the line sources is tailored to provide a greater flux near the center of the FOV, where the attenuation from the patient is greater. As the line sources decay, two new line sources are inserted into the center of the array. The rest of the lines are moved outward one position, and the weakest pair removed. The transmission profiles result from the overlapping irradiation of the individual lines, which varies with the distance of the source from the detector. The multiple line-source array provides full irradiation across the FOV of the parallel-hole collimator employed for emission imaging without the need for translation of the source, as did use of a sheet source. Supporting, shielding, and collimating the source array is not quite as cumbersome as it was for the sheet source, but is still more so than for a single line or point source. A major advantage of the configuration is that no scanning motion of the sources is required. A major disadvantage of this system is the amount of cross-talk between the emission and transmission photons. Due to Compton scattering within the patient, scatter from whichever is higher in energy will contaminate the energy window for the other.

As shown in Figure 10C, the sheet or multiple-line transmission source can be replaced by a scanning-line source [33]. The camera head opposed to the line source is electronically windowed to store only the events detected in a narrow region opposed to the line source in the transmission image. The electronic window moves in synchrony with the line thereby allowing transmission imaging across the entire FOV. The result is a significant reduction in the amount of scattered transmission radiation imaged in the transmission energy window. The transmission counts are concentrated in this moving spatial window thereby increasing their relative contribution compared to the emission events. Similarly using the portion of the FOV outside the transmission electronic window for emission imaging results in a significant reduction in the amount of cross-talk between transmission and emission imaging. Despite the significant reduction is cross-talk afforded by the scanning-line source methodology, compensation is still required for the residual cross-talk. The scanning-line source does have the disadvantage of requiring synchronized mechanical motion of the source with the electronic windowing employed to accept the transmission photons. The result can be an irradiation of the opposing head that changes with gantry angle, or erratically with time. Also, communication and synchronization between the camera and moving the line source can be problematic. However, the advantages of this method compared to its disadvantages are such that it is currently the dominant configuration offered commercially.

The need for lateral motion of the transmission source can be avoided, without the need for a cumbersome sheet or multiple-line source, if convergent collimation is employed. Figure 10D depicts the use of a fan-beam collimator with a line transmission source at its focal distance [34-36]. This configuration has the advantages that: 1) near "good geometry" attenuation coefficients are measured since the collimator acts as an anti-scatter grid, 2) convergent collimators provide a better spatial resolution sensitivity combination for small structures such as the heart than achieved with parallel collimation for emission imaging, and 3) only line or point sources need to be handled, shielded, or mounted on the system. The potential disadvantages of this configuration are: 1) an increased truncation of the FOV over that of parallel collimation on the same camera head, 2) the lack of electronic windowing to assist in correction of cross contamination between emission and transmission imaging, 3) the need to keep the source at the convergence location of the collimation, and 4) the emission images are acquired by fan-beam collimators. The latter distorts the projection images that physicians employ to look for breast shadows and lung uptake. Also, use of fan-beam collimators raises the possibility that both the transmission and emission projections of the heart may be truncated at some projection angles. One way around this on multi-headed SPECT systems is to do emission imaging with parallel-hole collimators on the heads that are not involved in transmission imaging [37]. The transmission source can be mounted on the system under motorized computer control to move the source radially with motion on the opposed camera head, thereby allowing body contouring acquisitions and overcoming this difficulty. With sequential transmission and emission imaging there is no need to correct the emission images for the presence of the transmission source. Also, images acquired in the transmission window during emission imaging can be used to estimate the contamination of the transmission images with transmission source present by the emission photons. One disadvantage of sequential scanning is an increase in the potential for patient motion that can result in misalignment between the emission and transmission images, and introduces artifacts [38]. Methods have been developed to estimate the contamination of emission and transmission images by the other source of radiation when simultaneous emission and transmission imaging is employed [34-36, 39, 40]. Thus, the influence of cross-contamination can be greatly reduced.

The major remaining potential problem with using convergent collimation for estimation of attenuation maps is that of truncation. Truncation of attenuation profiles results in the estimated attenuation maps exhibiting the "cupping artifact". This artifact is the result of the pile up of information from the truncated region near its edge when the reconstruction is limited to reconstructing only the region within the FOV at every angle. This region is called the fully sampled region (FSR). If the reconstruction is not limited to the FSR, then the "cupping artifact" is not present, but the area outside the FSR is distorted and inside the FSR is slightly reduced in value. Significant improvement can be obtained by constraining the reconstruction to the actual area of the attenuator [37]. Since the goal of transmission imaging is to estimate attenuation maps for the correction of attenuation in the emission images, the important question is not whether the maps are distorted by truncation, but rather whether the correction of attenuation is degraded by truncation. It has been reported that even though the attenuation map is significantly distorted outside the FSR, the attenuation sums (exponentials of the sums of the attenuation coefficients times path lengths) for locations in the FSR are estimated fairly accurately with iterative reconstruction [34, 36]. This is due to the iterative reconstruction algorithms employed in transmission reconstruction forcing the total attenuation across the maps to be consistent with the measured attenuation profiles, and to all locations being viewed at least part of the time. Thus, for structures such as the heart, which are within the FSR, a reasonably accurate AC can be obtained. Recently, it has been shown that truncation may have an impact on the detection of cardiac lesions [41]. Since both emission and transmission data were truncated in that work, it is unclear whether the decrease in the area under the

ROC curve was caused primarily by one, by the other, or by a combination of both types of truncation. There is no question, however, that truncation poses a serious problem for the AC of structures that are outside of the FOV at some angles.

Truncation can be eliminated, or at least dramatically reduced, by imaging with an asymmetric as opposed to a symmetric fan-beam collimator [42-45]. As shown in Figure 10E, use of asymmetric collimation results in one side of the patient being truncated, instead of both. By rotating the collimator 360^0 around the patient, conjugate views will fill in the region truncated. If a point source with electronic collimator is employed instead of a line source, then a significant improvement in cross-talk can be obtained [46]. Other benefits are that point sources cost less than line sources, and are easier to shield and collimate. The problem remains, however, that converging collimators acquire the emission profiles. This difficulty can be overcome, as illustrated in Figure 10F, by using photons from a medium-energy scanning-point source to create an asymmetric fan-beam transmission projection through a parallel-hole collimator by penetrating the septa of the collimator [47]. With this strategy, transmission imaging is performed sequentially after emission imaging to avoid transmission photons from contaminating the emission data. This lengthens the period of time that the patient must remain motionless on the imaging table. Another problem with this method of transmission imaging is that it really is only useful for imaging with low-energy parallel-hole collimators. For imaging medium-energy and high-energy photon emitters, an asymmetric fan-beam collimator would need to be employed.

Alternatives to transmission imaging for the estimation of attenuation maps do exist. One method used with cardiac perfusion imaging is to inject Tc-99m macroaggregated albumin (MAA) after the delayed images and then reimage the patient. The lung region is obtained by segmentation of the MAA localization, and the body outline is obtained either by an external wrap soaked in Tc-99m [48], or by segmentation of scatter-window images [49]. Assigning attenuation coefficients to the soft tissue and lung regions then forms the attenuation map. This method has the advantage of requiring no modification of the SPECT system to perform transmission imaging; however, a second pharmaceutical must be administered, and additional imaging must be performed. Another method of estimating attenuation maps without the use of transmission imaging is to segment the body and lung regions from scatter and photopeak energy window emission images of the imaging agent itself. This would not require any significant alteration or addition to present SPECT systems and imaging protocols beyond the simultaneous acquisition of a scatter window. Application of this method in patient studies has shown that approximate segmentation of the lung can be achieved interactively in many, but not all, patients [50]. This lack of robustness has limited its clinical use. The emission data does contain information regarding photon attenuation, and efforts have been made at extracting information on the attenuation coefficients directly from the emission data. One approach for doing so is to iteratively solve for both the emission and attenuation maps from the emission data [51, 52]. Another approach is to use the consistency conditions of the attenuated Radon transform to assist in defining an attenuation map that would affect the emission projections in the same way as the true attenuation distribution [53].

B. Compensation methods for correction of non-uniform attenuation

Not only has the ability to estimate attenuation maps improved greatly during the last decade, but so has the ability to perform AC once the attenuation maps are known. In part this is due to the tremendous changes in computing power, making computations practical which could only be performed as research exercises ten years ago. It is also due to an improvement in the algorithms used for correction and the efficiency of their implementations. An example is the development of ordered-subset or block-

iterative algorithms for use with maximum-likelihood reconstruction [54, 55]. Numerous AC algorithms have been proposed and investigated. For example, considerable effort has been directed towards the direct analytical solution for attenuation as part of reconstruction. Solutions to the Exponential Radon transform (uniform attenuation within a convex attenuator) have been derived [56-60]. These have been extended to correction of a convex region of uniform attenuation within a non-uniform attenuator [61-63]. Recently the Attenuated Radon transform, in the general case of non-uniform attenuation, has been analytically solved [64]. Any comprehensive review of AC algorithms would require a chapter dedicated solely to this task. Therefore, we will discuss at length only the two most commonly used AC algorithms: the Chang algorithm [65] used with FBP, and use of AC with the maximum-likelihood expectation-maximization reconstruction algorithm (MLEM) [67, 68]. The reader is referred to other reviews for more details and other algorithms [69-71].

To compare the algorithms we will make use of the 3D mathematical cardiac-torso (MCAT) phantom developed at the University of North Carolina at Chapel Hill [1]. Source and attenuation maps from the MCAT phantom were input to the SIMIND Monte Carlo simulation of gamma camera imaging [72]. SIMIND formed 128 x 128 pixel images for 120 angles about the source maps as imaged by a low-energy high-resolution parallel-hole collimator imaging Tc-99m. The primary and scatter components were recorded separately. This allowed the study of scatter-free images, that is images upon which "perfect" scatter compensation (SC) had been performed.

A simulation was made in which only the distance-dependent spatial resolution was simulated. This served as an example of "perfect" AC. Figure 11 shows the transverse slices and polar maps for 180^0 and 360^0 FBP reconstructions of this simulation. The slices were filtered pre-reconstruction with a 2D Butterworth filter of order 5.0 and cutoff frequency of 0.4 cycles/cm (0.125 of sampling frequency), as recommended for Tc-99m sestamibi rest images [73]. Notice the absence of the artifacts outside the heart in the transverse slices. Also, notice the uniformity of counts in the polar map aside from the band of increased counts due to the joining of left ventricle (LV) and right ventricle (RV), and the decrease in counts at the apex. These deviations from uniformity illustrate the impact of the partial-volume effect on the uniformity of cardiac wall counts. Where the wall is thicker, as with the joining of the RV and LV, the apparent counts will be higher. Where the wall is thinner, as with apical thinning (which was included in the simulated LV), the apparent counts will be lower. Thus, even with perfect AC and SC, one would not expect the wall of the LV to be uniform. Note also that there is slightly better uniformity of counts in the 360^0 reconstruction than the 180^0 reconstruction due to less variation in spatial resolution.

Figure 12 shows a transverse slice through the heart and "Bull's-eye" polar map for 180^0 and 360^0 FBP reconstructions of the slices with no AC when attenuation was included in the simulation. Again, 2D Butterworth filtering of order 5.0 and a cutoff frequency of 0.4 cycles/cm were employed. Notice the artifacts outside the heart due to the reconstruction of inconsistent projections, and the variation in intensity of the LV walls. The polar maps in this figure illustrate the fall-off in counts from the apex to the base due to the increase in attenuation with depth into the body. A decrease in the anterior wall due to the breast attenuation for 180^0 reconstruction is observed. Notice the slightly better uniformity of the 360^0 reconstruction due to the reduction in the impact of projection inconsistencies by combining opposing views. The goal of AC is to return the reconstructed distributions of Figure 12 to those of Figure 11.

The best known and widest employed of methods that perform AC with FBP is due to Chang [65]. The multiplicative or zeroth-order Chang method is a post-reconstruction correction method which seeks to compensate for attenuation by multiplying each point in the body by the reciprocal of the TF, averaged over acquisition angles, from the point to the edge of the body. That is, one calculates the correction factor (C(x' , y')) for each (x' , y') location in the slice as:

$$C(x', y') = \left[\frac{1}{M} \sum_{i=1}^{M} TF(t', s', \theta_i) \right]^{-1}, \tag{6}$$

where M is the number of projection angles θ_i, TF is calculated as per Equation 3, and Equation 1 is used to convert x' and y' into t' and s' for each θ_i. The correction is approximate because the TF's are not separable from the activity when summing over angle [74]. An iterative correction can be obtained in the following way. The zeroth-order corrected slices are projected, mathematically simulating the process of imaging, and the resulting estimated profiles subtracted from the actual emission data. Error slices are reconstructed from the differences using FBP. After correction of the error slices for attenuation in the same manner as the zeroth-order correction, the error slices are added to the zeroth-order estimate of the slices to obtain the first-order estimate. Typically only the first-order correction is performed, but the process can be repeated any number of times to obtain higher-order estimates. One problem with doing this is that the method does not converge (i.e., reaches a definite solution and then not changing with further iteration). Instead, the higher-order estimates are characterized by elevated noise [75]. Figure 13 shows MCAT transverse slices and polar maps for zeroth, first, and fifth-order Chang using the true non-uniform attenuation map to form the correction factors. Notice the considerable improvement of the poor correction of zeroth-order Chang after a single iteration. With five iterations, notice the increased noise evident in the slice and polar map.

As detailed in a previous chapter statistically based reconstruction algorithms start with a model for the noise in the emission data and then derive an estimate of the source distribution based on some statistical criterion. In maximum-likelihood expectation-maximization (MLEM), the noise is modeled as Poisson, and the criterion is to determine the source distribution that most likely gave the emission data using the expectation-maximization (EM) algorithm [67, 68]. The advantages of MLEM which have lead to its popularity include: 1) it has a good theoretical base; 2) it converges; 3) it readily lends itself to the incorporation of the physics of imaging such as attenuation; and 4) it compensates for non-uniform attenuation with a high degree of accuracy [76].

$$f_j^{new} = \frac{f_j^{old}}{\sum_i h_{ij}} \sum_i \left(h_{ij} \frac{g_i}{\sum_k h_{ik} f_k^{old}} \right) \tag{7}$$

The MLEM algorithm is given in equation 7, and works in the following way. First, as represented in the denominator on the right side of equation 7, projections are made by summing the current (old) estimate of the voxel counts (f^{old}) for each slice voxel k which contributes to projection pixel i. The initial estimate is typically a uniform count in each voxel. The weights used when summing the voxel counts (h_{ik}) are the probabilities that a photon emitted in voxel k contributes to projection pixel i. These probabilities form a matrix (H) called the transition matrix. H has the number of voxels as the number of columns, and the number of pixels in the projections as the number of rows. Thus for reconstruction of a 64 x 64 x 64 source distribution being acquired into 64 x 64 projections at 64 angles, H would be a 64^3 x 64^3 matrix. Each column in H is the unnormalized PSF for each acquisition angle stacked one on top of another for the associated voxel. If we form a column vector out of the voxel counts, then projection is

given by the matrix multiplication of H times this vector with the result being a column vector made up of the counts in each projection pixel. It is in this process of projecting (mathematically emulating imaging) that one includes the physics of imaging. For example, to include attenuation each h_{ik} would be formed as the product of the TF as calculated by equation 3 times the fractional contribution of voxel k to pixel i based on the geometry used to model imaging. In reality because of size one would not typically calculate and save the entire H matrix for 3D imaging. Instead, the needed terms are calculated "on-the-fly" by a procedure such as the following. Projecting along rows or columns is computationally inexpensive. Arbitrary projection angles can be placed in this orientation by appropriately rotating the estimated emission voxel slices and attenuation maps [77]. Given an aligned attenuation map for an estimate of an emission slice, one could include attenuation by starting with the voxel on the side opposite the projection being created and multiplying its value by the TF for passing through one-half the voxel distance of an attenuator of the given attenuation coefficient. The value of one-half the pixel dimension is usually used as an approximation for the self-attenuation of the activity in the voxel. One would then move to the next voxel along the direction of projection and add its value after correction for self attenuation to the current projection sum attenuated by passing through the entire thickness of the voxel. One would then continue this process until having passed through all voxels along the path of projection. The result of the projection operation is an estimate of the counts in pixel i based on the current estimate of the voxel counts, and the model of imaging being used in the transition matrix. As shown by the division on of the right side of equation 7, this estimate is then divided into the actual number of counts acquired in each pixel i. The ratio of the two indicates if the voxels along the given path of projection are too large (ratio below one), just right (ratio of one), or too small (ratio larger than one). These ratios are then backprojected as indicated by the summing over i in equation 7, to create an update for the estimate of voxel j. This update is the result of letting each ratio vote with a weight of h_{ij} on how the current estimate of voxel j should be altered. Note that the summing is now over the first subscript as opposed to the second as before. Thus, in terms of matrix algebra, we would be multiplying by the transpose of H in the backprojection operation. The update is multiplied times the current voxel estimate to obtain the updated estimate after normalization by dividing by the backprojection of 1.0's (division just to the right of the equal sign in equation 7).

The ordered-subset version of the MLEM algorithm (OSEM) [54] has accelerated reconstruction to the extent that clinically acceptable reconstruction times are now possible. With OSEM, one divides the projections into disjoint subsets. One then updates the estimate of the source distribution using just the projections within the given subset. A single iteration is complete after updating has occurred for all the subsets. The success of OSEM is such that it is now being used routinely for selected applications instead of FBP.

Figure 14 shows a comparison of the transverse slices and polar maps in the first column for 30 iterations of MLEM using the 180^0 of data from RAO to LPO, in the middle column for 30 iterations of MLEM using all 360^0 data, and at the right 100 iterations using all 360^0 data. All the reconstructions were 3D post-reconstruction filtered with a Butterworth filter with order of 5.0 and cut-off frequency of 0.64 cycles/cm. This cut-off is higher than the 0.4 cycles/cm used with all the FBP reconstructions. Notice that all three yield excellent reconstructions; however, 180^0 reconstruction is noisier (especially in the-low count areas behind the heart) and the uniformity of the polar map is slightly inferior compared to the 360^0 reconstructions. At 100 iterations, the noise has slightly increased, somewhat better resolution is apparent in the transverse slice, and the polar map is a little less uniform than at 30 iterations probably, due to the better resolution.

C. Impact of non-uniform attenuation compensation on image quality

AC is required for accurate absolute quantitation of activity [78]. In addition to its altering quantitation, attenuation is a major cause of artifacts in SPECT slices as discussed earlier. Thus, it is of interest to determine if AC can improve diagnostic accuracy in SPECT imaging. An area that has received a lot of attention as a candidate for the application of AC is cardiac perfusion imaging. Even though the need for AC from a physics point of view seems clear, the number of clinical studies reporting negative or equivocal results from the application of AC in perfusion imaging has lead to skepticism concerning its ultimate utility [79, 80]. Two papers do show the potential for improvement in diagnostic accuracy with AC. LaCroix et al. [81] conducted a ROC investigation using the MCAT phantom. They observed an improvement in defect detection when using AC with MLEM as opposed to FBP without AC, particularly for simulated patients with large breasts or a raised diaphragm. Ficaro, et al. [82] conducted a ROC investigation of AC in 60 patients who had undergone angiography. When coronary artery disease was defined as greater than 50 % stenoses in the luminal diameter, the area under the ROC curve increased from 0.734 with no AC to 0.932 with AC. Thus there is reason to believe that ultimately AC will be determined to make a significant contribution to improving the diagnostic accuracy of perfusion imaging. Recently a position statement reviewing the literature and summarizing the current view of AC in cardiac imaging has been published [83].

The question of the impact of attenuation and its compensation on tumor-detection accuracy is of significant current clinical interest [84]. Both positive [85] and negative [86] results have been reported as to the benefit of AC for F-18 labeled 2-fluror-2-deoxy-D-glucose (FDG). Thus, there does not appear to be a definitive answer yet as to the role of AC in tumor detection for PET FDG imaging.

Using simulated Ga-67 citrate SPECT imaging of the thorax for lymphoma, we [87] performed a localization receiver operating characteristics (LROC) comparison of: 1) FBP reconstruction with no AC; 2) FBP reconstruction with multiplicative Chang AC; 3) FBP with one iteration of iterative Chang AC; 4) one iteration of OSEM with no AC; and 5) one iteration of OSEM with AC. The "free" parameters for each of the five strategies were optimized using preliminary LROC studies. To compare the strategies, 200 lesion sites were randomly selected from a mask of potential lymphoma locations. 100 of these were used in observer training and strategy optimization, and 100 were used in data collection with 5 physician observers. In this study 3 different lesion contrasts were investigated; each image set contained an even distribution of lesion contrasts. We determined that AC does not significantly alter detection accuracy with FBP reconstruction. However, there was a significant improvement in detection accuracy when AC was included in OSEM (aggregate areas under the LROC curves (A_L) of 0.43, 0.39, 0.41, 0.41, and 0.58 for FBP no AC, FBP multiplicative Chang, FBP iterative Chang, OSEM no AC, and OSEM with AC, respectively). There were statistically significant differences between OSEM with AC and the other 4 reconstruction strategies for the aggregate, and also for two lower lesion contrasts. Numerically, OSEM with AC resulted in a larger A_L than did the other 4 strategies at the highest contrast considered, but the difference was no longer statistically significant. We believe this is an indication that once a lesion is of high enough contrast, OSEM with AC no longer provides a significant improvement in performance because there is little room for improvement as many of the lesions are obvious to begin with. We hypothesize that our positive finding for OSEM with AC is due in part to the use of the LROC methodology with no repetition of lesion locations in the comparison. This prevented the observers from memorizing the impact of attenuation artifacts on lesion appearance during training. Patient and lesion-site variability would also limit the physician's ability to do this clinically. Thus we believe that AC may improve tumor detection accuracy in SPECT imaging, especially when the tumors are in low-count

regions in slices which also contain significant concentrations of the imaging agent. AC would then help clean up attenuation artifacts, which spread from the high-count regions and interfere with detection.

III. Scatter Compensation

The imaging of scattered photons degrades contrast and signal-to-noise ratio (SNR), and must be accounted for if attenuation compensation (AC) is to be accurate [88, 89]. The methods for estimating attenuation maps available commercially try to estimate "good geometry" attenuation coefficients. In the past, the use of an effective (reduced) attenuation coefficient approximately accounted for the presence of scattered as well as primary photons in the projections when performing AC. The coefficient was typically selected to under correct the primary content of the emission projections so that a uniform reconstruction of a tub with a uniform concentration of activity resulted when projections with both primary and scatter were reconstructed [90]. The use of an effective attenuation coefficient to compensate for the presence of scatter is only, at best, a very approximate solution since the scatter distribution that is detected depends not only on the attenuator but also on the source distribution. Patient-activity distributions do not generally approximate a tub uniformly filled with activity. Thus instead of using an effective attenuation coefficient it is better to perform both SC and AC in conjunction since they are a team.

The best way to reduce the effects of scatter would be to improve the energy resolution of the imaging systems by using an alternative to the NaI(Tl) scintillator so that few scattered photons are acquired [5]. Figure 15 shows an energy spectrum obtained using the SIMIND Monte Carlo simulation package [72] for an LAO view of the 3D MCAT with the source distribution that of a Tc-99m sestamibi perfusion study as illustrated in Figure 9. Notice the finite width Gaussian response for the primary photons due to the finite energy resolution of the system, and the presence of scattered photons under this peak. The energy resolution (%FWHM) for the NaI(Tl) camera in this simulation was set at 10%. Figure 16 shows a plot of how the scatter fraction varies for %FWHM's of 1% to 10% when a symmetric window of width twice that of the %FWHM is employed in imaging. Note that both classical and Compton scattering were included in the simulation. From the plot it is evident that even with 1% energy resolution there would still be a small amount of scatter imaged. Besides improving energy resolution to have less scatter within the imaging window, one can alter the placement of the energy window over the photopeak so that it covers less of the region below the peak itself [91]. This reduces the amount of scatter collected, but also reduces the number of primary photons.

A number of SC algorithms have been proposed for SPECT systems that employ NaI(Tl) detectors. Generally, the methods of SC can be divided into two different categories [92, 93]. The first category, which we will call scatter estimation, consists of those methods that estimate the scatter contributions to the projections based on the acquired emission data. The data used may be information from the energy spectrum or a combination of the photopeak data and an approximation of scatter PSF's. The scatter estimate can be used for SC before, during, or after reconstruction. The second category consists of those methods that model the scatter PSF's during the reconstruction process. The second approach will be called reconstruction-based scatter compensation (RBSC) herein.

A. Scatter estimation methods

The difficulty in scatter estimation is illustrated in Figure 17 which shows that the acquired projection data is the result of the contributions from primary photons, scattered photons, and noise. In scatter estimation one tries to obtain an accurate estimate of the scatter distribution avoiding any biases.

However, even if this is obtained, then its removal from the acquired projection would still leave the noise inherent in the detection of the scattered photons behind. Thus scatter estimation methods typically reduce the bias in the projections due to scatter, but enhance the noise level.

Energy-distribution-based methods seek to estimate the amount of scatter in a photopeak-energy-window pixel by using the variation of counts acquired, in the same pixel, in one or more energy windows. The pixel-based nature of this method allows for the generation of a scatter estimate for each pixel in the photopeak-window data. The Compton window subtraction method [94] is the classic example of this strategy. In this method, a second energy window placed below the photopeak window is used to record a projection consisting of scattered photons. This projection is multiplied by a scaling factor k, and is then subtracted from the acquired projection to yield a scatter-corrected projection. This method assumes that the spatial distribution of the scatter within the Compton scatter window is the same as that within the photopeak window, and that once it is determined from a calibration study, a single scaling factor holds true for all applications on a given system. That the distribution of scatter in the two windows differs can be seen by noting that the average angle of scattering (and hence the degree of blurring) changes with energy. Also, the value of k varies depending on radionuclide, energy-window definition, pharmaceutical distribution, region of the body and other factors [95].

Making the scatter window smaller and placing it just below the photopeak window can minimize the difference in the distribution of scatter between it and the photopeak window. With this arrangement, one obtains the two-energy window variant of the triple-energy window (TEW) SC method [96]. The two-energy window variant is useful when downscatter from a higher energy photon is not present as in the case of imaging solely Tc-99m. In this method, the scatter in a pixel is estimated as the area under a triangle whose height is the average count per keV in the window below the photopeak window, and whose base is the width of the photopeak window in keV. When downscatter is present, a third small window is added above the photopeak as illustrated in Figure 18 [97]. With the addition of this third window, scatter is estimated as the area under the trapezoid formed by the heights of the counts per keV in each of the two narrow windows on either side of the photopeak, and a base with the width of the photopeak window. By making the windows smaller, one estimates the scatter distribution from regions of the energy spectrum closer to the photopeak window thereby improving the correspondence of the scattered-photon energies with those in the photopeak window. The price paid for this is that the estimation is based on fewer counts and therefore is noisier. Thus heavy low-pass filtering of the scatter estimate is required to reduce the noise in the estimate [98].

Energy-distribution based methods that use a limited number of energy windows to estimate the primary counts do not completely compensate for scatter. This is in part due to their use of simple geometric shapes to estimate the scatter within the photopeak window. The main advantages of such methods are their speed and simplicity for clinical use. Performance can be improved through the use of more windows, which would allow a greater degree of freedom when estimating the scatter within the photopeak window. A number of investigators have developed multi-window methods [99-101]. The problem with methods that require more than a few energy windows is that the required number of windows is not available on many SPECT systems. Also, dividing the spectrum up into a large number of windows decreases the detected counts in each window, thus increasing the noise in the windows.

Another subclass of scatter-estimation methods is the spatial-distribution-based methods. These methods seek to estimate the scatter contamination of the projections on the basis of the acquired photopeak window data, which serves as an estimate of the source distribution, and a model of the blurring of the source into the scatter distribution. The latter is typically an approximation to the scatter PSF, an illustration of which for one location in the 3D MCAT phantom is shown in Figure 19. Beck and

colleagues [102] conducted an early analysis of the contribution of scatter to the response observed for point and line sources.

An example of a spatial-distribution method for SC in SPECT is the convolution-subtraction method, which modeled the scatter response as decreasing exponentially from its center maximum value [103]. The center value and slope of the exponential were obtained from measurements made with a finite length line source. This function was convolved with the acquired projection data, and the result was used as an estimate of the scatter distribution in the projection. The estimated distribution was subtracted from the original data to yield scatter corrected projection data. One problem with this method was it assumed that the scatter model did not change with location. To overcome this problem, Monte Carlo methods were used to generate a set of scatter responses that were, in turn, used to interpolate the scatter response at a given location [104]. Both of these approaches used scatter line-spread functions (LSF's) instead of PSF's. That is, the source modeled was a finite length line instead of a point. Convolution was performed one-dimensionally in the plane of the slice to be reconstructed. Scatter originating outside the plane was assumed to be included as a result of using the finite length line.

Msaki, et al., [105] modeled the two-dimensional (2D) scatter PSF and performed 2D convolution to account for across-plane scatter as well as in-plane scatter. This method was further refined by adapting the scatter PSF for the individual patient using photon transmission through an attenuation map [106, 107]. Convolution-subtraction methods offer a fast and reasonably accurate way of correcting for scatter. Their main disadvantages are: the subtraction of the scatter estimate elevates noise in the primary estimate, the accuracy with which the scatter PSF is modeled is often poor, and the estimation of scatter from sources not within the field of view of the camera poses a problem.

B. Reconstruction-based scatter compensation (RBSC) methods

RBSC starts with the estimated source and attenuation distributions and calculates the contribution of scatter to the projections by using the underlying principles of scattering interactions. With RBSC methods compensation is achieved, in effect, by mapping scattered photons back to their point of origin instead of trying to determine a separate estimate of the scatter contribution to the projections [93]. All of the photons are used in RBSC, and it has been argued that there should be less noise increase than with the other category of compensation [92,93]. One disadvantage, which RBSC shares with the convolution-based subtraction method discussed in the previous section, is that RBSC does not allow for the direct calculation of scatter from sources that are outside of the reconstructed field of view.

The accuracy of RBSC however depends on the accuracy of modeling scatter, and accurate modeling of scatter is computation intensive. As with AC, the estimation of accurate patient-specific attenuation maps is essential since they are used to form the patient-specific scatter PSF's. It is also vital that inter-slice (3D) as well as intra-slice (2D) SC be performed [108-110]. Thus, for reconstruction of a 64 x 64 x 64 source distribution imaged at 64 angles one would need to form a transition matrix consisting of 64^4 PSF's each consisting of 64 x 64 terms, or 64.7 x 10^9 terms in total. Since each patient presents a unique attenuation distribution, the transition matrix used in reconstruction ideally should be formed for the individual patient. Such a transition matrix could be obtained by manufacturing an attenuation distribution which matches the patient's, and in which a point source can be positioned independently in each voxel to allow measurement of the PSF's. However, the point source imaging time is prohibitive for routine clinical use, and the storage in memory and on disk of such a matrix represents a significant problem even by today's hardware standards. Thus, the terms in the matrix are normally calculated as needed without saving them, and with various levels of approximation. Also, the

contribution of scatter to the projections may be calculated directly without the actual formation of the PSF's as in the case of Monte Carlo simulation.

For the case of a uniform, convex attenuator a parallel/serial model of the system PSF can be used to separate the distance-dependent camera response from the depth-dependent scatter response [13, 14, 111]. In this approach a distance-dependent Gaussian is used to model the system response to the primary photons. A second Gaussian is used to model the depth-dependent scatter response originating from the attenuator. This scatter response is convolved with the appropriate system response for the distance from the collimator since the two are in series, and summed after scaling with the response of the primary photons, since primary and scatter are modeled as being imaged in parallel. The scaling is based on the scatter-to-primary ratio (scatter fraction) for the given depth in the attenuator. In this way PSF's can be quickly formed from the storage of just the regression models of the variation of the FWHM of the primary photons with distance, the scattered photons with depth, and the scatter fraction with depth.

The difficulty with the parallel/serial approach as described above is that it accounted for only variations in the depth of the source and not variations in the attenuator to either side of the path of the primary photons to the camera. This approach was refined by including parameterization of the scatter response as a function of the shape of the uniform attenuator relative to the position of the point source [112, 113]. The result were system PSF's which matched measured PSF's in uniform, convex attenuators exceedingly well, but were not suitable for use with non-uniform attenuation. An attempt was made to allow these slab derived scatter responses to account for non-uniform attenuation, but the estimated responses did not achieve the same level of agreement as with the case of uniform attenuation [114, 115].

An alternative approach is to calculate the scatter response by integration of the Klein-Nishina formula for Compton scattering using the patient's attenuation maps for the attenuator distribution [116, 117]. By calculating the PSF's analytically as opposed to stochastically these methods achieve "noise-free" estimates in a fixed amount of time unlike Monte Carlo simulation methods where noise in the estimate and calculation time are directly linked. Since the processing time increases dramatically with the order of the scatter interactions, only first (scattering once before detection) and second (scattering twice before detection) order scatter are typically included in the calculation. The processing time can also be reduced by factoring the calculation so that a significant amount of it can be contained in precalculated camera-dependent look-up tables. These methods result in excellent agreement with experimental and Monte Carlo PSF's. For point sources, the computation times are significantly faster than with Monte Carlo simulation. This advantage over Monte Carlo however, is dependent on the source configuration and is lost for large, extended source distributions.

Still another approach is based on the calculation of an effective scatter source from which the contribution of scatter to the projections can be estimated using the same projector as for the primary photons [93, 118-120]. With this approach the estimated primary distribution is blurred into an effective scatter source distribution. The effective scatter source is formed by taking into account the probability that a photon emitted at a given location will reach the scattering site, that the photon there undergoes a scattering interaction which leads to it being detected, and finally that the scattered photon will interact in the crystal producing an event which is within the energy window used in imaging. The probability of it not being lost due to attenuation on its way from its last scattering site to the crystal is handled by the attenuated projector. By making some approximations in the calculation, excellent agreement with Monte Carlo simulation can be obtained in reconstruction times feasible for clinical use. For one method, the approximations made in order to attain this speed include assuming spatial invariance so that the blurring kernels can be precalculated by Monte Carlo simulation, and truncating a Taylor series expansion of the exponential describing the probability of attenuation of the photon from the site of emission to the site of

last scattering [93, 118]. With use of Monte Carlo precalculated kernels, the path of the photon from emission to last scattering interaction before detection can include scattering interactions up to any order desired. However, these intermediate scatterings are assumed to occur in a uniform medium. An alternative method formulates the effective scatter source distribution by incrementally blurring and attenuating each layer of the patient forward towards the detector [119, 120]. The attenuation coefficients from the estimated attenuation map are used to do the layer by layer attenuation, thus this method does not assume a uniform medium when correcting for the attenuation from the site of emission to scattering. The incremental blurring is however based on a Gaussian approximation to first-order Compton scattering as calculated from the Klein-Nishina equation. Thus only first-order scatter makes up between 80% and 90% of the scattering events in the Tc-99m photopeak window are included. The effective scatter source image is created from the result of the incremental blurring and attenuation through multiplication by the voxel attenuation coefficient. This effective scatter source image is then incrementally projected taking into account attenuation and system spatial resolution to produce the estimate of scatter in the projection. In this final stage the alteration of the attenuation coefficient resulting from the change in the energy of the photons upon scattering is not accounted for.

One final approach to including scatter in making the projections from the estimate of the source distribution during reconstruction is Monte Carlo simulation. Monte Carlo simulation was one of the first methods investigated for this purpose [121,122]. However, until very recently it was too slow to consider for clinical use. This is no longer the case. Beekman and colleagues have developed a Monte Carlo approximation which can perform 10 iterations of OSEM using an unmatched projector/backprojector on a dual processor PC in 10 minutes for a 64 x 64 x 64 reconstruction of a Tc-99m distribution [123]. The largest portion of the speed increase was obtained by combining stochastic photon transport of the interactions within the patient with an analytical model of the detection by the camera, a technique they call convolution-based forced detection [124]. In this method the photon weight and the location of its last interaction in the patient are stored. Upon completion of the Monte Carlo simulation of each projection angle, the weights are grouped together according to their distance from the camera, convolved with the system PSF for that distance, and projected. This process accelerates Monte Carlo simulation by a factor of about fifty times. One can think of this as going back to the serial model of imaging where Monte Carlo simulation of interactions within the patient are in series with an analytical model of the camera.

A number of changes in the iterative reconstruction algorithm have been combined with the above approaches with the result that the inclusion of 3D modeling of scatter during reconstruction is now possible in clinically feasible time frames. Such algorithmic improvements include the development of acceleration methods based on the updating of the reconstruction estimate by subsets of the data as previously discussed under the AC section [54, 55, 125]. The use of an unmatched projector/backprojector pair greatly speeds reconstruction allowing one to only model scattering in the projection operation [125-127]. One can also use coarse-grid scatter modeling, and either hold the scatter contribution fixed after a few iterations or update the scatter projection intermittently during reconstruction [128].

C. Impact of scatter compensation on image quality

There is little question that SC is necessary for accurate activity quantitation [78]. However, the gains in contrast with SC are typically accompanied by altered noise characteristics so that the benefit for tumor-detection of SC is uncertain. Using contrast-to-noise plots for simulated Tc-99m images, Beekman et al. [92] compared ideal scatter rejection (the imaging of solely primary photons), ideal scatter estimation (provision of the actual scatter content in each projection bin), ideal scatter modeling (perfect

knowledge of the scatter PSF's, which is the ideal for the RBSC methods), and no SC. They determined that ideal scatter rejection was the best, followed by ideal scatter modeling, and then ideal scatter estimation. Similar results were reported by Kadrmas et al. [93] for Tl-201 cardiac imaging. They noted that they had not performed a study of differences in noise correlations between the methods, and that "such differences would be expected to affect the usefulness of reconstructed images for tasks such as lesion detection".

One method of accounting for noise correlation in a study of the impact of SC on image quality is to perform a human-observer ROC experiment. We have investigated the impact of scatter on "cold" and "hot" tumor detection for Tc-99m -labeled antibody fragments used for hepatic imaging [129, 130]. Prior to performing this investigation we hypothesized that scatter could: 1) degrade detection accuracy by decreasing contrast; 2) improve the accuracy of detection because it adds counts (information), some of which are in the correct location; or 3) have no impact because these two factors would cancel. The SIMIND Monte Carlo program [72] was used to create high-count SPECT projections of the abdominal region as defined by the Zubal phantom [131]. The primary and scattered photons were stored in separate data files. Similarly, high-count projections of a 2.5-cm diameter spherical "tumor" in each of 3 locations within the liver were also created via SIMIND. These projections were scaled and added to ("hot" tumors) or subtracted from ("cold" tumors) the background distribution. Projections were made with solely the primary photons present. These were used to assess the impact of perfect scatter rejection as might be approximated by imaging with a detector with extremely good energy resolution. Projections were also made with both the primary and scattered photons present (standard imaging of Tc-99m), and with 2.5 times the scattered Tc-99m photons present (an approximation to imaging with significantly more scattered photons as would occur with Ga-67). Multiple noise realizations of the projections with no tumor present were created. Multiple realizations were also made with tumors at each of three locations. Energy-window-based SC was applied to the noisy projections that contained scatter. The projections were 2D low-pass filtered with a Butterworth filter whose parameters matched those used clinically in our department. The projections were then reconstructed using FBP and multiplicative Chang AC. The negative values were truncated from the slices, and upper-thresholding to place the average value of a voxel in the liver at the center of the gray-scale was applied. A signal-known-exactly (SKE) ROC study was then conducted with 5 observers. The potential location of the tumor was indicated via removable crosshairs, and a continuous scale was used for the observers' confidence ratings. The LABROC1 program provided by Dr. Metz was used to estimate, from the ratings for each observer, a binormal ROC curve and the area under the curve (A_Z). Statistical analysis of the A_Z's indicated that only for the case of the "hot" tumors was there a statistically significant difference in detection accuracy between ideal scatter rejection (primary-only images), and the slices with the standard amount of scatter (uncorrected low-scatter case). In either case, the difference in A_Z's was small (0.88 versus 0.86 for cold tumors, and 0.84 versus 0.80 for hot tumors). For both tumor polarities, primary images gave a statistically significant increase in detection accuracy in comparison to the images with an artificially elevated amount of scatter. Here the difference in areas was larger (0.88 versus 0.81 for cold tumors, and 0.84 versus 0.74 for hot tumors). In no case did SC result in a statistically significant increase in detection accuracy over no compensation. However, with the artificially elevated amount of scatter the areas did increase with SC (0.81 with no compensation versus 0.83 with SC for the cold tumors, and 0.74 with no compensation versus 0.78 with SC for the hot tumors). These results indicate that scatter does decrease lesion detection accuracy, particularly when there is a significant amount of scatter present. They also suggest that scatter estimation methods may be able to improve lesion detection accuracy when there is a significant amount of scatter present. It awaits to be

seen whether RBSC methods are superior to estimation methods for undoing the impact of scatter on lesion detection.

IV. Spatial Resolution Compensation

A. Restoration filtering

For a shift-invariant linear system in the absence of noise, the image g(x,y) is the convolution of the object f(x,y) with the point spread function h(x,y), or [14]

$$g(x,y) = \int\int_{-\infty}^{\infty} f(x',y')\, h(x-x',y-y')\, dx'\, dy' \ . \tag{8}$$

By taking the 2D Fourier transform, Equation 8 can be expressed in the frequency domain as

$$G(u,v) = OTF(u,v) \cdot F(u,v) \ , \tag{9}$$

where OTF is the optical transfer function which specifies the changes in both the magnitude and phase of the frequency components of the object by the imaging system, and u and v are the spatial frequencies.

We can solve Equation 9 for F by dividing both sides by the OTF. Division by the OTF represents the inverse filter, and is an example of unregularized restoration filtering [132]. In restoration filtering one models the degradation (h or OTF), and applies the inverse process with the goal of recovering the original image. One problem with this approach, of course, is noise. For the case of spatially independent Poisson noise [133], Equation 9 can be written as:

$$G(u,v) = OTF(u,v) \cdot F(u,v) + N(u,v) \ , \tag{10}$$

where N is the contribution due to noise. For images degraded by Poisson noise the average value of the noise power spectrum (P_N), which is the complex magnitude squared of N ($\|N\|^2$), is a constant equal to the total number of counts in the image [133, 134]. The object power spectrum (P_F) decreases rapidly with frequency, and the multiplication by the OTF further decreases its contribution to G. Thus, one reaches a point as the frequency increases where N will be the dominant contributor to G. Application of the inverse filter will result in a significant amplification of the noise at such frequencies. In restoration filtering one usually follows the inverse filter at low frequencies, where the contributions of the signal dominate the image, and then switches to low-pass filtering to avoid excessive amplification of noise when the noise dominates. A number of filters have been proposed for regularizing restoration [132].

One such filter is the Wiener filter, which uses the minimization of the mean squared error as the criterion for filter design [134]. The Wiener filter can be written in the frequency domain as:

$$W(u,v) = \left(\frac{OTF^*(u,v)}{[OTF^2(u,v) + P_N(u,v)/P_F(u,v)]} \right) = \left(\frac{1}{OTF(u,v)} \right)\left(\frac{OTF^2(u,v)}{[OTF^2(u,v) + P_N(u,v)/P_F(u,v)]} \right), \tag{11}$$

where * indicates the complex conjugate. The right-hand side of Equation 11 explicitly shows the Wiener filter as the product of the inverse filter and a low-pass filter. To apply this filter one needs estimates of

P_N, P_F, and OTF. For 2D pre-reconstruction filtering of SPECT acquisition images, P_N can be estimates as the total image count, as stated above. However, for 3D post-reconstruction filtering, estimates of P_N need to be modified to account for the impact of reconstruction [135]. Once one has an estimate of P_N, an estimate of P_F can be obtained from the image power spectrum and knowledge of the OTF [111, 134-137]. One is then left with estimation of the OTF. The problem here is that the OTF varies with distance from the face of the collimator. Thus there is no single OTF that correctly models the blurring for all the structures in the image.

One solution to the problem of a distance-dependent OTF is to approximate it as distance-independent, using a single OTF evaluated at a distance equal to the mean free path of the photons being imaged [134]. A more accurate solution to the problem is offered by the frequency-distance relationship (FDR) [138]. The FDR states that in the 2D fast Fourier transform (FFT) of the sinogram, the amplitudes of the signal from any given distance relative to the center-of-rotation (COR) are concentrated along a line which runs through the origin in the frequency domain. That is:

Angular Frequency = - Distance • Spatial Frequency ,   (12)

with the negative of the distance being the slope of the line, or

Distance = - Angular Frequency / Spatial Frequency ,   (13)

where Distance is relative to the COR, so that the distance (d) from the camera face is COR + Distance. The FDR and the meaning of Equation 13 can be visualized with the aid of Figure 20. Figure 20 shows two straight lines oriented at 45^0 passing through the origin of the 2D FFT of the sinogram. Each of these lines represents a constant value of the ratio of the angular to spatial frequency, and therefore a specific distance from the COR. In the upper right quadrant of the 2D FFT, both the angular and spatial frequencies are positive. Any line which passes through the origin of the 2D FFT and is in this quadrant represents frequency locations at which the signal is concentrated at locations in the source distribution closer to the camera than the COR. This can be seen by noting that in this quadrant, by Equation 13, Distance is negative so that d is less than the COR. This quadrant is said to represent "near-field" locations. In the lower right quadrant, the angular frequencies are negative while the spatial frequencies are positive. This quadrant represents signal in the source emitted at distances farther away than the COR since now Distance will be positive. This region represents the "far-field" locations. Thus FDR allows one to know the distance from the camera at which the signal was emitted, with the exception of the origin through which all lines or distances pass. Since all OTF's should be 1.0 at this location, this does not represent a problem when applying the FDR to a single slice. By modeling the detector point spread function as a Gaussian function whose width is dependent on d as in Equation 5, spatially variant restoration filters have been developed [139, 140]. A 3D implementation is achieved by also Fourier transforming in the between-slice direction (z-axis of projections) [141]. A problem is encountered in determining what distance to use to select the OTF for deblurring the z-axis transform of the origin since all distances pass through this location. We have used the average source-to-detector distance for this purpose [141]. Using the FDR, the Wiener filter can be expressed as

$$W(u,v,w) = \left(\frac{1}{OTF(u,v,d)} \right) \left(\frac{OTF^2(u,v,d)}{[OTF^2(u,v,d) + P_N(u,v,w) / P_F(u,v,w)]} \right) , \qquad (14)$$

where w is the inter-slice or axial angular frequency in the 3D FFT of the sinograms, and d is the distance from the face of the collimator (COR - w/u). The FDR has been expanded to work with body contouring, as well as with circular camera orbits [142].

Application of the FDR to pre-reconstruction restoration filtering SPECT acquisitions has advantages in terms of computational load and being linear. It also has several disadvantages [143]. It is limited as to how much resolution recovery can be obtained without excessive amplification of noise. Under certain conditions, after FDR pre-reconstruction filtering, transverse slices will contain circular noise correlations [144]. Also, the FDR is an approximation, especially at low spatial frequencies. Finally, any form of pre-reconstruction filtering correlates the noise in the projections that will be input to reconstruction algorithms and MLEM assumes uncorrelated Poisson noise in the projection data.

B. Modeling spatial resolution in iterative reconstruction

Another method to correct for the distance-dependent camera response is the incorporation of a blurring model into iterative reconstruction [110-112, 145-149]. The problem with this method has been the immense increase in computational burden imposed when an iterative reconstruction algorithm includes such modeling in its transition matrix. The use of block-iterative reconstruction algorithms has been shown to dramatically reduce the number of iterations required to reconstruct slices [110, 150].

Blurring incrementally with distance using the method of Gaussian diffusion [151] can dramatically reduce the computational burden per iteration. With this method, system spatial resolution in the absence of scatter is modeled with a Gaussian function whose standard deviation (σ) varies with distance as per Equation 5. A special property of Gaussians is that the convolution of two Gaussians produces a Gaussian whose σ equals the square root of the sum of the squares the σ's of the original two Gaussians. Thus the system response at some distance d_{i+1} can be expressed as the convolution of the response at distance d_i with a Gaussian whose standard deviation (σ_{inc}) is given by

$$\sigma_{inc} = \left(\sigma_S^2(d_{i+1}) - \sigma_S^2(d_i) \right)^{1/2}. \tag{15}$$

The advantage of the incremental approach is that σ_{inc} is much smaller than $\sigma_S(d_{i+1})$ and thus requires a smaller-dimension mask to approximate the Gaussian (ie., less computation). In fact, one typically uses a mask made up of 3 terms to approximate the 1D incremental Gaussian. The first and third mask coefficients are the same due to the symmetry of Gaussians. Thus, 1D convolution can be implemented by summing the voxel values to either side of the center location of the mask, multiplying the result by the coefficient, and adding that result to the center voxel value multiplied by its coefficient. Making use of the separability of the Gaussian function, one can implement 2D convolution as a 1D horizontal convolution followed by a 1D vertical convolution. This requires only 4 multiplications and 4 additions per voxel. If a rotator is used to align the slices with the acquisition angles [77, 152], then the projection and backprojection steps can be implemented along columns (straight lines). The incremental steps in distance occur as one moves from one plane (distance from the camera) to the next. The projection can be implemented by convolving the farthest plane of the slices with the Gaussian for the increment in distance between that plane and the next plane closer to the detector. The result is then added to the next plane, and the sum is convolved with the Gaussian for the increment in distance to the next plane. The process is repeated until the plane nearest the detector is reached. The Gaussian for the distance between the detector and that plane is used in the final convolution. This will generally require a mask of larger than 3 terms to sample the Gaussian for this distance without significant truncation. The result is a projection in which the

blurring varies with distance such that the farthest planes are blurred the most. With backprojection, one would start by first blurring the projection for the distance between the detector and the first plane of slices, and incrementally blurring as one proceeds along the slice columns thereafter. Using a step size of larger than one row can further reduce computational time [153].

Using a 3-term mask to approximate a Gaussian can result in aliasing distorting the desired response [154]. For the Gaussian diffusion method [151], the mask can be determined from a linear difference equation approximation of the diffusion partial differential equation

$$\frac{\partial q}{\partial z} = \alpha^2 \left(\frac{\partial^2 q}{\partial x^2} + \frac{\partial^2 q}{\partial y^2} \right), \tag{16}$$

which describes the diffusion in the direction z (with a diffusion constant α^2) of the 3D activity distribution q(x,y,z). The Gaussian diffusion mask that approximates the blurring from the plane at distance d_i to the plane at d_{i+1} is ($\sigma^2_{inc}/2$, $1 - \sigma^2_{inc}$, and $\sigma^2_{inc}/2$) [151]. Use of these coefficients has been shown to minimize the impact of aliasing compared to alternative ways of defining the mask coefficients as a function of σ_{inc}[154].

Another way of decreasing the computational burden at each iteration is to model spatially variant resolution only in the projection step [126]. Zeng and Gullberg [127] have recently reported on conditions which are necessary in order to guarantee convergence of an iterative algorithm when the projector and backprojector are unmatched.

Even with all these computational enhancements, modeling the PSF in iterative reconstruction is still slower than restoration filtering. Furthermore, it results in reconstructions where the extent to which a stationary and isotropic response results depends on the location of the source, the camera orbit, the number of iterations used, the reconstruction algorithm, and the source distribution [150]. However, it does avoid the approximation inherent in the FDR, does not alter the noise characteristics of the projections prior to reconstruction, and has yielded significant improvements in resolution without a significant increase in noise [109].

C. Impact of resolution compensation on image quality

One of the major impacts of spatial resolution is manifested in the partial-volume effect. Tomographic systems have a characteristic "resolution volume" that is determined by their 3D PSF [5]. Objects smaller than the extent of the PSF only partially occupy this volume. Therefore, the count determined at that location only partially reflects the object since it also contains a contribution from structures beyond this object. The result is that the apparent concentration for objects smaller than 2 to 3 times the FWHM of the PSF will depend on the size and shape of the object as well as the concentration of activity within the object [155, 156], and the object will be spread out into a region in the slices larger than its true size [157]. Objects larger in size will have their concentration distorted near their edges by the partial-volume effect, and will be blurred out into the surrounding region. It has been observed that modeling of the PSF in iterative reconstruction can reduce the bias in quantitation better than can FDR-Wiener filtering [158]. However, there are limits to how far even modeling the system resolution in iterative reconstruction can go in correcting for the partial-volume effect. Thus alternative strategies for partial volume compensation are of great interest [27, 159].

One question of significant clinical importance is whether restoration filtering or modeling the PSF

in iterative reconstruction can improve the accuracy of lesion detection. We conducted an LROC investigation of this using the detection of tumors in simulated thoracic Ga-67 citrate SPECT slices as the task [160]. When the reconstruction and filtering parameters were optimized for our detection task, we determined that OSEM with AC and detector resolution compensation (DRC) significantly improves detection accuracy over that with either OSEM with AC alone, or OSEM with AC and FDR restoration filtering. In this investigation, five different reconstruction strategies were compared: 1) FBP with multiplicative Chang AC (current clinical practice); 2) OSEM with AC; 3) OSEM with AC and FDR restoration filtering; 4) OSEM with AC and Gaussian-Diffusion DRC (GD-DRC); and 5) OSEM with AC of data simulated with a stationary detector response which just limited aliasing ("ideal case"). The latter was investigated to serve as an upper limit for DRC. Figure 21 shows example reconstructions for several lesions for these 5 methods. Note that the visibility of tumors of the same contrast varies with location in the slices. This illustrates why we believe it is necessary to present lesions at numerous locations when assessing observer performance. A series of four observer studies, using 5 observers, was conducted. The first study compared the five methods for a single tumor contrast. The second investigated the impact of number of iterations of OSEM with GD-DRC on detection accuracy. The third compared lesion detection for OSEM with and without GD-DRC for 8 different lesion contrasts with observers reading images of a single contrast at a time. The fourth study compared the 5 reconstruction strategies for observers reading lesions of 3 different contrasts mixed together. In the fourth study the A_L for the 3 contrasts in aggregate were 0.55, 0.67, 0.67, 0.77, and 0.99, for the 5 methods, respectively. Note the tremendous difference between current clinical practice and the ideal case we investigated. Also notice that OSEM with AC and GD-DRC is able to improve detection to approximately halfway between the two. All differences between pairs of methods were statistically significant except OSEM with AC versus OSEM with AC and FDR restoration filtering. An interesting observation in this study was that the number of iterations of OSEM for which the highest detection accuracy was achieved increased from 1 iteration with 8 subsets of 16 angles each for OSEM with AC to 8 iterations of 16 subsets of 8 angles each for OSEM with AC and GD-DRC. That is, more faithfully modeling the physics of imaging in the transition matrix employed in iterative reconstruction resulted in an increased number of iterations and improved detection. Eight iterations was the number determined to be optimal in the preliminary optimization studies. In the second observer study reported in the paper [159], 6 iterations resulted in a numerically, but not statistically, larger A_L. Eight (or even 6) iterations of OSEM with AC and GD-DRC for 128 by 128 images is time consuming.

Our results for the improvement in detection accuracy with GD-DRC for simulated Ga-67 citrate images indicates that there may be a significant clinical impact from using modeling of the PSF with iterative reconstruction. It remains to be seen whether such an improvement is seen clinically, and whether improvements in detection are observed for other clinical procedures. A significant improvement in image quality was reported for modeling the PSF in SPECT imaging of F-18 [161]. Similarly, modeling the PSF was observed to improve quantitative measures of image quality for cardiac imaging [162, 163] and brain imaging [164]; however, it has yet to be determined to what extent such modeling improves the detection of cardiac or brain lesions.

V. Conclusions

From this review we believe it should be evident that solely compensating for attenuation is not enough to improve SPECT image quality to its fullest extent. Instead, attenuation, scatter, and resolution as well as correction of patient and physiological motion, and changes in localization during the course of

acquisition can impact image quality, and thus combined compensation is required. It is our opinion that as a result of improvements in algorithms and computer hardware, the best way to perform such compensations is to accurately model the degradations in iterative reconstruction. Evidence is beginning to be obtained that these compensations do significantly improve the diagnostic utility of SPECT images. For example, in an ROC study of the accuracy of detection of coronary disease using cardiac-perfusion SPECT imaging with clinical images, we have recently determined that combined correction for attenuation, scatter, and spatial resolution is more accurate than FBP or solely AC, or AC and SC [165]. However, it should be remembered that the corrected images look different than the uncorrected images physicians have grown accustomed to reading. Thus it will require a period of adjustment for the clinicians to develop a new mental picture of what "normal" looks like before the full potential of the compensations is realized clinically [79, 166].

VI. Acknowledgments

VII. References

1. Tsui BMW, Zhao XD, Gregoriou, Lalush DS, Frey EC, Johnston RE, McCartney WH. Quantitative cardiac SPECT reconstruction with reduced image degradation due to patient anatomy. IEEE Trans Nucl Sci 41: 2838-2848, 1994.

2. Boas ML. Mathematical Methods in the Physical Sciences. Second Edition, John Wiley & Sons, New York, 1983.

3. Kak AC, Slaney M. Principles of Computerized Tomographic Imaging. IEEE Press, New York, 1987.

4. Attix FH. Introduction to Radiological Physics and Radiation Dosimetry. John Wiley & Sons, New York, 1983.

5. Sorenson JA, Phelps ME. Physics in Nuclear Medicine. Second Edition, Grune & Stratton, Orlando, 1987.

6. de Vries DJ, King MA. Window selection for dual photopeak window scatter correction in Tc-99m imaging. IEEE Trans Nucl Sci 41:2771-2778, 1994.

7. Hademenous GJ, King MA, Ljungberg M, Zubal G, Harrell CR. A scatter correction method for Tl-201 images: a Monte Carlo investigation. IEEE Trans Nucl Sci 30:1179-1186, 1993.

8. Metz CE, Atkins FB, Beck RN: The geometrical transfer function component for scintillation camera collimators with straight parallel holes. Phys Med Biol 25: 1059-1070, 1980.

9. Tsui BMW, Gullberg GT. The geometric transfer function for cone and fan beam collimators. Phys Med Biol 35: 81-93, 1990.

10. Frey EC, Tsui BMW, Gullberg GT. Improved estimation of the detector response function for converging beam collimators. Phys Med Biol 43: 941-950, 1998.

11. Formiconi AR. Geometrical response of multihole collimators. Phys Med Biol 43: 3359-3379, 1998.

12. Brookeman VA, Bauer TJ. Collimator performance for scintillation camera systems. JNM 14: 21-25, 1973.

13. Gilland DR, Tsui BMW, McCarthy WH, Perry JR, Berg J. Determination of the optimum filter function for SPECT imaging. JNM 29: 643-650, 1988.

14. Metz CE, Doi K: Transfer function analysis of radiographic imaging. Phys Med Biol 24: 1079-1106, 1979.

15. Manglos SH, Jaszczak RJ, Floyd CE, Hahn LJ, Greer KL, Coleman RE. A quantitative comparison of attenuation-weighted backprojection with multiplicative and iterative postprocessing attenuation compensation in SPECT. IEEE Trans Med Imag 7:128-134, 1988.

16. King MK, Xia W, de Vries DJ, Pan T-S, Villegas BJ, Dahlberg S, Tsui BMW, Ljungberg MH, Morgan HT. A Monte Carlo investigation of artifacts caused by liver uptake in single-photon emission computed tomography perfusion imaging with Tc-99m labeled agents. J Nucl Card 3:18-29, 1996.

17. Germano G, Chua T, Kiat H, Areeda JS, Berman DS. A quantitative phantom analysis of artifacts due to hepatic activity in technetium-99m myocardial perfusion SPECT studies. J Nucl Med 35:356-359, 1994.

18. O'Connor MK, Kelly BJ. Evaluation of techniques for the elimination of "hot" bladder artifacts in SPECT of the pelvis. J Nucl Med 31: 1872-75, 1990.

19. Gillen GJ, Gilmore B, Elliott AT. An investigation of the magnitude and causes of count loss artifacts in SPECT imaging. JNM 32: 1771-1776, 1991.

20. Nuyts J, Dupont P, Van den Maegdenbergh V, Vleugels S, Suetens P, Mortelmans L. A study of liver-heart artifact in emission tomography. J Nucl Med 36:133-139, 1995.

21. Jaszczak RJ, Chang LT, Stein NA, Moore FE. Whole-body single-photon emission computed tomography using dual, large-field-of-view scintillation cameras. Phys Med Biol 24:1123-1143, 1979.

22. King MA, Tsui BMW, Pan T-S. Attenuation compensation for cardiac single-photon emission computed tomographic imaging: Part 1. Impact of attenuation and methods of estimating attenuation maps. J Nucl Card 2:513-524, 1995.

23. Fleming JS. A technique for using CT images in attenuation correction and quantification in SPECT. Nucl Med Comm 10:83-97, 1989.

24. Meyer CR, Boes JL, Kim B, Bland PH, Zasadny KR, Kison PV, Koral K, Frey KA, Wahl RL. Demonstration of accuracy and clinical versatility of mutual information for automatic multimodality image fusion using affine and thin-plate spline warped geometric deformations. Med Imag Anal 1:195-206, 1996.

25. Blankespoor SC, Wu X, Kalki K, Brown JK, Tang HR, Cann CE, Hasegawa BH. Attenuation correction of SPECT using x-ray CT on an emission-transmission CT system: myocardial perfusion assessment. IEEE Trans Nucl Sci 43:2263-2274, 1996.

26. LaCroix KJ, Tsui BMW, Hasegawa BH, Brown JK. Investigation of the use of x-ray CT images for attenuation compensation in SPECT. IEEE Trans Nucl Sci 41:2793-2799, 1994.

27. Da Silva AJ, Tang HR, Wong KH, Wu MC, Dae MW, Hasegawa BH. Absolute quantification of regional myocardial uptake of Tc-99m- sestamibi with SPECT: experimental validation in a porcine model. J Nucl Med 42:772-779, 2001.

28. Maeda H, Itoh H, Ishii Y, Makai T, Todo G, Fujita T, Torizuka K. Determination of the pleural edge by gamma-ray transmission computed tomography. JNM 22:815-817, 1981

29. Malko JA, Van Heertum RL, Gullberg GT, Kowalsky WP. SPECT liver imaging using an iterative attenuation correction algorithm and an external flood source. JNM 26:701-705, 1985.

30. Bailey DL, Hutton BF, Walker PJ. Improved SPECT using simultaneous emission and transmission tomography. JNM 28:844-851, 1987.

31. Cao ZJ, Tsui BMW. Performance characteristics of transmission imaging using a uniform sheet source with a parallel-hole collimator. Med Phys 19:1205-1212, 1992.

32. Celler A, Sitek A, Stoub E, Hawman P, Harrop R, Lyster D. Multiple line source array for SPECT transmission scans: simulation, phantom, and patient studies. JNM 39:2183-2189, 1998.

33. Tan P, Bailey DL, Meikle SR, Eberl S, Fulton RR, Hutton BF. A scanning line source for simultaneous emission and transmission measurements in SPECT. JNM 34:1752-1760, 1993.

34. Tung C-H, Gullberg GT, Zeng GL, Christian PE, Datz FL, Morgan HT. Nonuniform attenuation correction using simultaneous transmission and emission converging tomography. IEEE Trans Nucl Sci 39:1134-1143, 1992.

35. Jaszczak RJ, Gilland DR, Hanson MW, Jang S, Greer KL, Coleman RE. Fast transmission CT for determining attenuation maps using a collimated line source, rotatable air-copper-lead attenuators and fan-beam collimation. JNM 34:1577-1586, 1993.

36. Gullberg GT, Morgan HT, Zeng GL, Christian PE, Di Bella EVR, Tung C-H, Maniawski PJ, Hsieh Y-L, Datz FL. The design and performance of a simultaneous transmission and emission tomography system. IEEE Trans Nucl Sci 45:1676-1698, 1998.

37. Narayanan MV, King MA, Pan T-S, Dahlberg ST. Investigation of approaches to reduce truncation of attenuation maps with simultaneous transmission and emission SPECT imaging. IEEE Trans Nucl Sci 45:1200-1206, 1998.

38. Stone CD, McCormick JW, Gilland DR, Greer KL, Coleman RE, Jaszczak RJ. Effect of registration errors between transmission and emission scans on a SPECT system using sequential scanning. JNM 39:365-373, 1998.

39. Barnden LR, Ong PL, Rowe CC. Simultaneous emission transmission tomography using technetium-99m for both emission and transmission. EJNM 24:1390-1397, 1997.

40. Narayanan MV, King MA, Byrne CL. An iterative transmission algorithm incorporating cross-talk correction for SPECT. Med Phys 29:694-700, 2002.

41. Gregoriou GK, Tsui BMW, Gullberg GT. Effect of truncated projections on defect detection in attenuation-compensated fanbeam cardiac SPECT. JNM 39:166-175, 1998.

42. Chang W, Loncaric S, Huang G, Sanpitak P. Asymmetric fan transmission CT on SPECT systems. Phys Med Biol 40:913-928, 1995.

43. Gilland DR, Jaszczak RJ, Greer KL, Coleman RE. Transmission imaging for nonuniform attenuation correction using a three-headed SPECT camera. JNM 39:1005-1110, 1998.

44. Hollinger EF, Loncaric S, Yu D-C, Ali A, Chang W. Using fast sequential asymmetric fanbeam transmission CT for attenuation correction of cardiac SPECT imaging. JNM 1335-1344, 1998.

45. LaCroix KJ, Tsui BMW. Investigation of 90 dual-camera half-fanbeam collimation for myocardial SPECT imaging. IEEE Trans Nucl Sci 46:2085-2092, 1999.

46. Beekman FJ, Kamphuis C, Hutton BF, van Rijk PP. Half-fanbeam collimators combined with scanning point sources for simultaneous emission-transmission imaging. JNM 39:1996-2003, 1998.

47. Gagnon D, Tung CH, Zeng L, Hawkins WG. Design and early testing of a new medium-energy transmission device for attenuation correction in SPECT and PET. Proceed 1999 Med Imag Conf, IEEE, 2000, Paper M8-3.

48. Madsen MT, Kirchner PT, Edlin JP, Nathan MA, Kahn D. An emission-based technique for obtaining attenuation correction data for myocardial SPECT studies. Nucl Med Comm 14:689-695, 1993.

49. Wallis JW, Miller TR, Koppel P. Attenuation correction in cardiac SPECT without a transmission measurement. JNM 36:506-512, 1995.

50. Pan T-S, King MA, Luo D-S, Dahlberg ST, Villegas BJ. Estimation of attenuation maps from scatter and photopeak window single photon emission computed tomographic images of technetium-99m labeled sestamibi. J Nucl Card 4:42-51, 1997.

51. Manglos SH, Young TM. Constrained IntraSPECT reconstruction from SPECT projections. Proceed 1993 MIC. 1605-1609, 1994.

52. Nuyts J, Dupont P, Stroobans S, Benninck R, Mortelmans L, Suetens P. Simultaneous maximum a posteriori reconstruction of attenuation and activity distributions from emission sinograms. IEEE Trans Med Imag 18:393-403, 1999.

53. Welch A, Clack R, Natterer F, Gullberg GT. Toward accurate attenuation correction in SPECT without transmission measurements. IEEE Trans Med Imag 16:532-541, 1997.

54. Hudson HM, Larkin RS. Accelerated image reconstruction using ordered subsets of projection data. IEEE Trans Med Imag 13: 601-609, 1994.

55. Byrne CL. Accelerating the EMML algorithm and related iterative algorithms by rescaled block-iterative methods. IEEE Trans Imag Proc 7:100-109, 1998.

56. Bellini S, Piacentini M, Cafforio C, Rocca F. Compensation of tissue absorption in emission tomography. IEEE Trans Acou Sp Sig Proc 27:213-218, 1979.

57. Tretiak O, Metz C. The exponential Radon transform. SIAM J Appl Math 39:341-354, 1980.

58. Gullberg GT, Budinger TF. The use of filtering methods to compensate for constant attenuation in single-photon emission computed tomography. IEEE Trans Biomed Eng 28:142-157, 1981.

59. Hawkins WG, Leichner PK, Yang NC. The circular harmonic transform for SPECT reconstruction and boundary conditions on the Fourier transform of the sinogram. IEEE Trans Med Imag 7:135-148, 1988.

60. Metz CE, Pan X. A unified analysis of exact methods of inverting the 2-D exponential Radon transform, with implications for noise control in SPECT. IEEE Trans Med Imag 14:643-657, 1995.

61. Markoe A. Fourier inversion of the attenuated x-ray transform. SIAM J Math Anal 15:718-722, 1984.

62. Liang Z, Ye J, Harrington DP. An analytical approach to quantitative reconstruction of non-uniform attenuated SPECT. Phys Med Biol 39:2023-2041, 1994.

63. Glick SJ, King MA, Pan T-S, Soares EJ. An analytical approach for compensation of non-uniform attenuation in cardiac SPECT imaging. Phys Med Biol 40:1677-1693, 1995.

64. Natterer F. Inversion of the attenuated Radon transform. Inver Prob 17:113-119, 2001.

65. Chang LT. A method for attenuation correction in radionuclide computed tomography. IEEE Trans Nucl Sci 25:638-643, 1978.

67. Shepp LA, Vardi Y. Maximum likelihood reconstruction for emission tomography. IEEE Trans Med Imag 1:113-122, 1982.

68. Lange K, Carson R. EM reconstruction algorithms for emission and transmission tomography. J Comp Assist Tomo 8:306-316, 1984.

69. Parker JA. Quantitative SPECT: Basic theoretical considerations. Sem Nucl Med 19:3-13, 1989.

70. Tsui BMW, Zhao XD, Frey EC, McCartney WH. Quantitative Single-Photon Emission Computed Tomography: Basics and Clinical Considerations. Seminars Nucl Med 24:38-65, 1994.

71. King MA, Tsui BMW, Pan T-S, Glick SJ, Soares EJ. Attenuation compensation for cardiac single-photon emission computed tomographic imaging: Part 2.Attenuation compensation algorithms. J Nucl Card 3:55-63, 1996.

72. Ljungberg M, Strand S-E. A Monte Carlo program for the simulation of scintillation camera characteristics. Comp Meth Prog Biomed 29:257-272, 1989.

73. Garica EV, Cooke CD, Van Train KF, Folks R, Peifer J, DePuey EG, Maddahi J, Alazraki N, Galt J, Ezquerra N, Ziffer J, Areeda J, Berman DS. Technical aspects of myocardial SPECT imaging with technetium-99m sestamibi. Amer J Card 66:29E-31E, 1990.

74. Singh M, Horne M, Maneval D, Amartey J, Brechner R. Non-Uniform Attenuation and Scatter Correction in SPECT. IEEE Trans Nucl Sci 35:767-71, 1988.

75. Lalush DS, Tsui BMW. Improving the Convergence of Iterative Filtered Backprojection Algorithms. Med Phys 21:1283-5, 1994.

76. Chornoboy ES, Chen CJ, Miller MI, Miller TR, Snyder DL. An evaluation of maximum likelihood reconstruction for SPECT. IEEE Trans Med Imag 9:99-110, 1990.

77. Wallis JW, Miller TR. An optimal rotator for iterative reconstruction. IEEE Trans Med Imag 16: 118-123, 1997.

78. Rosenthal MS, Cullom J, Hawkins W, Moore SC, Tsui BMW, Yester M. Quantitative SPECT imaging: a review and recommendations by the focus committee of the society of nuclear medicine computer and instrumentation council. JNM 36:1489-1513, 1995.

79. Watson DD, Germano G, DePuey EG, et al. Report summary of Wintergreen panel on instrumentation and quantification. J Nucl Card 6:94-103, 1999.

80. Hendel RC, Berman DS, Cullom SJ, et al. Multicenter clinical trial to evaluate the efficacy of correction for photon attenuation and scatter in SPECT myocardial perfusion imaging. Circul 99:2742-2749, 1999.

81. LaCroix KJ, Tsui BMW, Frey EC, Jaszczak RJ. Receiver operating characteristic evaluation of iterative reconstruction with attenuation correction in Tc-99m sestamibi myocardial SPECT images. JNM 41:502-513, 2000.

82. Ficaro EP, Fessler JA, Shreve PD, et al. Simultaneous transmission/emission myocardial perfusion tomography: Diagnostic accuracy of attenuation-corrected Tc-99m-sestamibi single-photon emission computed tomography. Circ 93:463-473, 1996.

83. Hendel RC, Corbett JR, Cullom J, DePuey EG, Garcia EV, Bateman TM. The value and pratice of attenuation correction for myocardial perfusion SPECT imaging: A joint position statemant from the American Society of Nuclear Cardiology and the Society of Nuclear Medicine. J Nucl Card 9:135-143, 2002.

84. Whal RL. To AC or not to AC: That is the question. JNM 40: 2025-2028, 1999.

85. Chan MT, Leahy RM, Mumcuoglu EU, Cherry SR, Czernin J, Chatziioannou A. Comparing lesion detection performance for PET image reconstruction algorithms: a case study. IEEE Trans Nucl Sci 44: 1558-1563, 1997.

86. Farquhar TH, Llacer J, Hoh CK, et. al.. ROC and Localization ROC analyses of lesion detection in whole-body FDG PET: Effects of acquisition mode, attenuation correction and reconstruction algorithm. JNM 40:2043-2052, 1999.

87. Wells RG, King MA, Simkin PH, Judy PF, Brill AB, Gifford HC, Licho R, Pretorius PH, Schneider P, Seldin DW. Comparing filtered backprojection and ordered-subsets expectation maximization for small lesion detection and localization in Ga-67 SPECT. J Nucl Med. 41:1391-1399, 2000.

88. Jaszczak RJ, Coleman RE, Whitehead FR. Physical factors affecting quantitative measurements using camera-based single photon emission computed tomography (SPECT). IEEE Trans Nucl Sci 28:69-80, 1981.

89. Jaszczak RJ, Whitehead FR, Lim CB, Coleman RE. Lesion detection with single-photon emission computed tomography (SPECT) compared with conventional imaging. J Nucl Med 23: 97-102, 1982.

90. Harris CC, Greer KL, Jaszczak RJ, Floyd CE, Fearnow EC, Coleman RE. Tc-99m attenuation coefficients in water-filled phantoms determined with gamma cameras. Med Phys 11:681-685, 1984.

91. Atkins FB, Beck RN, Hoffer PN, Palmer D. Dependence of optimum baseline setting on scatter fraction and detector response function. In, <u>Medical Radioisotope Scintigraphy</u>. IAEA, 101-118, 1968.

92. Beekman FJ, Kamphuis C, Frey EC. Scatter compensation methods in 3D iterative SPECT reconstruction: A simulation study. Phys Med Biol 42: 1619-1632, 1997.

93. Kadrmas DJ, Frey EC, Tsui BMW. Application of reconstruction-based scatter compensation to thallium-201 SPECT: implementations for reduced reconstruction image noise. IEEE Trans Med Imag 17: 325-333, 1998.

94. Jaszczak RJ, Greer KL, Floyd CE Jr, Harris CC and Coleman RE. Improved SPECT quantitation using compensation for scattered photons. J Nucl Med 25:893-900, 1984.

95. Koral KF, Swailem FM, Buchbinder S, Clinthorne NH, Rogers WL, Tsui BMW. SPECT dual-energy-window Compton correction: scatter multiplier required for quantification. J Nucl Med 31:90-98, 1990.

96. Ogawa K, Ichihara T, Kubo A. Accurate scatter correction in single photon emission CT. Ann Nucl Med Sci 7:145-150, 1994.

97. Ogawa K, Harata Y, Ichihara T, Kubo A and Hasimoto S. A practical method for position-dependent Compton-scatter correction in single photon emission CT. IEEE Med Imag 10:408-412, 1991.

98. King MA, de Vries DJ, Pan T-S, Pretorius PH, Case JA. An investigation of the filtering of TEW scatter estimates used to compensate for scatter with ordered subset reconstructions. IEEE Trans Nucl Sci 44: 1140-1145, 1997.

99. Koral KF, Wang XQ, Rogers WL, Clinthorne NH, Wang X. SPECT Compton-scattering correction by analysis of energy spectra. JNM 29:195-202, 1988.

100. Gagnon D, Todd-Pokropek A, Arsenault A, Dapras G. Introduction to holospectral imaging in nuclear medicine for scatter subtraction. IEEE Trans Med Imag 8:245-250, 1989.

101. Haynor DR, Kaplan MS, Miyaoka RS, Lewellen TK. Multiwindow scatter correction techniques in single-photon imaging. Med Phys 22:2015-2024, 1995.

102. Beck RN, Schuh MW, Cohen TD, Lembares N. Effects of scattered radiation on scintillation detector response. In, <u>Medical Radioisotope Scintigraphy</u>. IAEA, 595-616, 1968.

103. Axelsson B, Msaki P, Israelsson. Subtraction of Compton-scattered photons in single-photon emission computed tomography. JNM 25:490-494, 1984.

104. Ljungberg M, Strand S-E. Attenuation and scatter correction in SPECT for sources in nonhomogenous object: a Monte Carlo study. JNM 32: 1278-1284, 1991.

105. Msaki P, Axelsson B, Dahl CM, Larsson SA. Generalized scatter correction method in SPECT using point scatter distribution functions. JNM 28: 1861-1869, 1987.

106. Meikle SR, Hutton BF, Bailey DL. A transmission-dependent method for scatter correction in SPECT. JNM 35:360-367, 1994.

107. Hutton BF, Osieck A, Meikle SR. Transmission-based scatter correction of 180^0 myocardial single-photon emission tomographic studies. EJNM 23:1300-1308, 1996.

108. Munley MT, Floyd CE Jr, Tourassi GD, Bowsher JE, and Coleman RE. Out-of-plane photons in SPECT. IEEE Trans Nucl Sci 38:776-779, 1991.

109. Tsui BMW, Frey EC, Zhao XD, Lalush DS, Johnston RE, McCartney WH. The Importance and Implementation of Accurate 3D Compensation Methods for Quantitative SPECT. Phys Med Bio 39:509-30, 1994.

110. Kamphuis C, Beekman FJ, Viergever MA. Evaluation of OS-EM vs. ML-EM for 1D, 2D and fully 3D SPECT reconstruction. IEEE Trans Nucl Sci 43: 2018-2024, 1996.

111. Penny BC, King MA, Knesaurek K. A projector, back-projector pair which accounts for the two-dimensional depth and distance dependent blurring in SPECT. IEEE Trans Nucl Sci 37: 681-686, 1990.

112. Beekman FJ, Eijkman EGJ Viergever MA, Born GF, Slijpen ETP. Object shape dependent PSF model for SPECT imaging. IEEE Trans Nucl Sci 40: 31-39, 1993.

113. Frey EC, Tsui BMW. A practical method for incorporating scatter in a projector-backprojector for accurate scatter compensation in SPECT. IEEE Trans Nucl Sci 40: 1107-1116, 1993.

114. Frey EC, Tsui BMW. Modeling the scatter response function in inhomogeneous scattering media for SPECT. IEEE Trans Nucl Sci 41: 1585-1593, 1994.

115. Beekman FJ, den Harder JM, Viergever MA, van Rijk PP. SPECT scatter modelling in non-uniform attenuating objects. Phys Med Biol 42: 1133-1142, 1997.

116. Riauka TA, Gortel ZW. Photon propagation and detection in single-photon emission computed tomography – an analytical approach. Med Phys 21: 1311-1321, 1994.

117. Wells RG, Celler A, Harrop R. Analytical calculation of photon distributions in SPECT projections. IEEE Trans Nucl Sci 45:3202-3214, 1998.

118. Frey EC, Tsui BMW. A new method for modeling the spatially-variant, object-dependent scatter response function in SPECT. Proceed 1966 MIC, 1082-1086, 1997.

119. Zeng GL, Bai C, Gullberg GT. A projector/backprojector with slice-to-slice blurring for efficient three-dimensional scatter modeling. IEEE Trans Med Imag 18: 722-732, 1999.

120. Bai C, Zeng GL, Gullberg GT. A slice-by-slice blurring model and kernel evaluation using the Klein-Nishina formula for 3D scatter compensation in parallel and convergent beam SPECT. Phys Med Biol 45: 1275-1307, 2000.

121. Floyd CE, Jaszczak RJ, Coleman RE. Inverse Monte Carlo: a unified reconstruction algorithm. IEEE Trans Nucl Sci 32: 799-785, 1985.

122. Bowsher JE, Floyd CE. Treatment of Compton scattering in maximum-likehppd, expectation-maximization reconstructions of SPECT images. JNM 32: 1285-1291, 1991.

123. Beekman FJ, de Jong HWAM, van Geloven S. Efficient fully 3D iterative SPECT reconstruction with Monte Carlo based scatter compensation. IEEE Trans Med Imag, submitted.

124. de Jong HWAM, Slijpen ETP, Beekman FJ. Acceleration of Monte Carlo SPECT simulation using convolution-based forced detection. IEEE Trans Nucl Sci 48:58-64, 2001.

125. Kamphuis C, Beekman FJ, van Rijk PV, Viergever MA. Dual matrix ordered subsets reconstruction for accelerated 3D scatter compensation in single-photon emission tomography. EJNM 25:8-18, 1998.

126. Zeng GL, Gullberg GT. Frequency domain implementation of the three-dimensional geometric point response correction in SPECT imaging. IEEE Trans Nucl Sci 39: 444-453, 1992.

127. Zeng L, Gullberg GT. Unmatched projector/backprojector pairs in an alternative iterative reconstruction algorithm. IEEE Trans Med Imag 19:548-555, 2000.

128. Kadrmas DJ, Frey EC, Karimi SS, Tsui BMW. Fast implementations of reconstruction-based scatter compensation in fully 3D SPECT image reconstruction. Phys Med Biol 43:857-873, 1998.

129. de Vries DJ, King MA, Tsui BMW, Metz CE. Evaluation of the effect of scatter correction on lesion detection in hepatic SPECT Imaging. IEEE Trans Nucl Sci 44:1733-1740, 1997.

130. de Vries DJ, King MA, Soares EJ, Tsui BMW, Metz CE. Effects of scatter subtraction on detection and quantitation in hepatic SPECT. JNM 40: 1011-1023, 1999.

131. Zubal IG, Harrell CR, Smith EO, Rattner Z, Gindi G, Hoffer PB. Computerized three-dimensional segmented human anatomy. Med Phys 21:299-302, 1994.

132. Gonzalez RC, Woods RE. Digital Image Processing. Addison-Wesley Pub Co, Reading, 1992, pp 253-305.

133. Goodman JW, Belsher JF. Fundamental limitations in linear invariant restoration of atmospherically degraded images. Proceed SPIE 75:141-154, 1976.

134. King MA, Doherty PW, Schwinger RB. A Wiener filter for nuclear medicine images. Med Phys

10:876-880, 1983.

135. King MA, Schwinger RB, Doherty PW, Penney BC. Two-dimensional filtering of SPECT images using the Metz and Wiener filters. JNM 25:1234-1240, 1984.

136. Penney BC, Glick SJ, King MA. Relative importance of the error sources in Wiener restoration of scintigrams. IEEE Trans Med Imag 9:60-70, 1990.

137. Madsen MT. A method for obtaining an approximate Wiener filter. Med Phys 17:126-130, 1990.

138. Edholm PR, Lewitt RM, Lindholm B. Novel properties of the Fourier decomposition of the sinogram. Proc SPIE 671: 8-18, 1986.

139. Lewitt RM, Edholm PR, Xia W. Fourier method for correction of depth-dependent collimator blurring. Proc SPIE 1092:232-243, 1989.

140. Hawkins WG, Yang N-C, Leichner PK. Validation of the circular harmonic transform (CHT) algorithm for quantitative SPECT. JNM 32:141-150. 1991.

141. Glick SJ, Penney BC, King MA, Byrne CL. Noniterative compensation for the distance-dependent detector response and photon attenuation in SPECT imaging. IEEE Trans Med Imag 13: 363-374, 1994.

142. Xia W, Lewitt RM, Edholm PR. Fourier correction for spatially variant collimator blurring in SPECT. IEEE Trans Nucl Sci 14: 100-115, 1995.

143. Kohli V, King MA, Glick SJ, Pan T-S. Comparison of frequency-distance relationship and Gaussian-diffusion based methods of compensation for distance-dependent spatial resolution in SPECT imaging. Phys Med Biol 43:1025-1037, 1998.

144. Soares EJ, Glick SJ, King MA. Noise characterization of combined Bellini-type attenuation correction and frequency-distance principle restoration filtering. IEEE Trans Nucl Sci 43:3278-3290, 1996.

145. Floyd CE, Jaszczak RJ, Manglos SH, Coleman RE. Compensation for collimator divergence in SPECT using inverse Monte Carlo reconstruction. IEEE Trans Nucl Sci 35:784-787, 1988.

146. Tsui BMW, Hu H-B, Gilland DR, Gullberg GT. Implementation of Simultaneous Attenuation and Detector Response Correction in SPECT. IEEE Trans Nucl Sci 35:778-83, 1988.

147. Formiconi AR, Pupi A, Passeri A. Compensation of spatial response in SPECT with conjugate gradient reconstruction technique. Phys Med Biol 34: 69-84, 1989.

148. Zeng GL, Gullberg GT, Tsui BMW, Terry JA. Three-Dimensional Iterative Reconstruction Algorithms with Attenuation and Geometric Point Response Correction. IEEE Trans Nucl Sci 38:693-702, 1991.

149. Liang Z. Compensation for attenuation, scatter, and detector response in SPECT reconstruction via iterative FBP methods. Med Phys 20:1097-1106, 1993.

150. Pan T-S, Luo D-S, Kohli V, King MA. Influence of OSEM, elliptical orbits, and background activity on SPECT 3D resolution recovery. Phys Med Biol 42: 2517-2529, 1997.

151. McCarthy AW, Miller MI. Maximum likelihood SPECT in clinical computation times using mesh-connected parallel computers. IEEE Trans Med Imag 10: 426-436, 1991.

152. Di Bella EVR, Barclay AB, Schafer RW. A comparison of rotation-based methods for iterative reconstruction algorithms. IEEE Trans Nucl Sci 43: 3370-3376, 1996.

153. Bai C, Zeng GL, Gullberg GT, DiFilippo F, Miller S. Slab-by-slab blurring model for geometric point response correction and attenuation correction using iterative reconstruction algorithms. IEEE Trans Nucl Sci 45:2168-2173, 1998.

154. King MK, Pan T-S, Luo D-S. An investigation of aliasing with Gaussian-diffusion modeling of SPECT system spatial resolution. IEEE Trans Nucl Sci 44:1375- 1380, 1997.

155. Hoffman EJ, Huang S-C, Phelps ME. Quantitation in positron emission computed tomography: 1. Effect of object size. J Comp Assist Tomo 3:299-308,1979.

156. Kessler RM, Ellis JR, Eden M. Analysis of emission tomographic scan data: limitations imposed by resolution and background. J Comp Assist Tomo 8:514-522, 1984.

157. King MA, Long DT, Brill AB. SPECT volume quantitation: influence of spatial resolution, source size and shape, and voxel size. Med Phys 18:1016-1024, 1991.

158. Pretorius PH, King MA, Pan T-S, de Vries DJ, Glick SJ, Byrne CL. Reducing the influence of the partial volume effect on SPECT activity quantitation with 3D modelling of spatial resolution in iterative reconstruction. Phys Med Biol 43:407-420, 1998.

159. Hutton BF, Osiecki A. Correction of partial volume effects in myocardial SPECT. J Nucl Cardiol 5:402-413, 1998.

160. Gifford HC, King MA, Wells RG, Hawkins WG, Narayanan MV, Pretorius PH. LROC analysis of detector-response compensation in SPECT. IEEE Trans Med Imag 19:463-473, 2000.

161. Zeng GL, Gullberg GT, Bai C, Christian PE, Trisjono F, Di Bella EVR, Tanner JW, Morgan HT. Iterative reconstruction of flourine-18 SPECT using geometric point response correction. JNM 39:124-130, 1998.

162. Kohli V, King MA, Pan T-S, Glick SJ. Compensation for distance-dependent resolution in cardiac-perfusion SPECT: impact on uniformity of wall counts and wall thickness. IEEE Trans Nucl Sci 45:1104-1110, 1998.

163. Hutton BF, Lau YH. Application of distance-dependent resolution compensation and post-reconstruction filtering for myocardial SPECT. Phys Med Biol 43:1679-1693, 1998.

164. Beekman FJ, Kamphuis C, Viergever MA. Improved SPECT quantitation using fully three-dimensional iterative spatially variant scatter response compensation. IEEE Trans Med Imag 15:491-499, 1996.

165. Narayanan MV, Pretorius PH, Dahlberg ST, Leppo J, Spencer F, King MA. Human observer ROC evaluation of attenuation, scatter and resolution compensation strategies for Tc-99m myocardial perfusion imaging. JNM 43:3P, 2002, abstract.

166. Hutton BF. Cardiac single-photon emission tomography: is attenuation correction enough? EJNM 24:713-715, 1997.
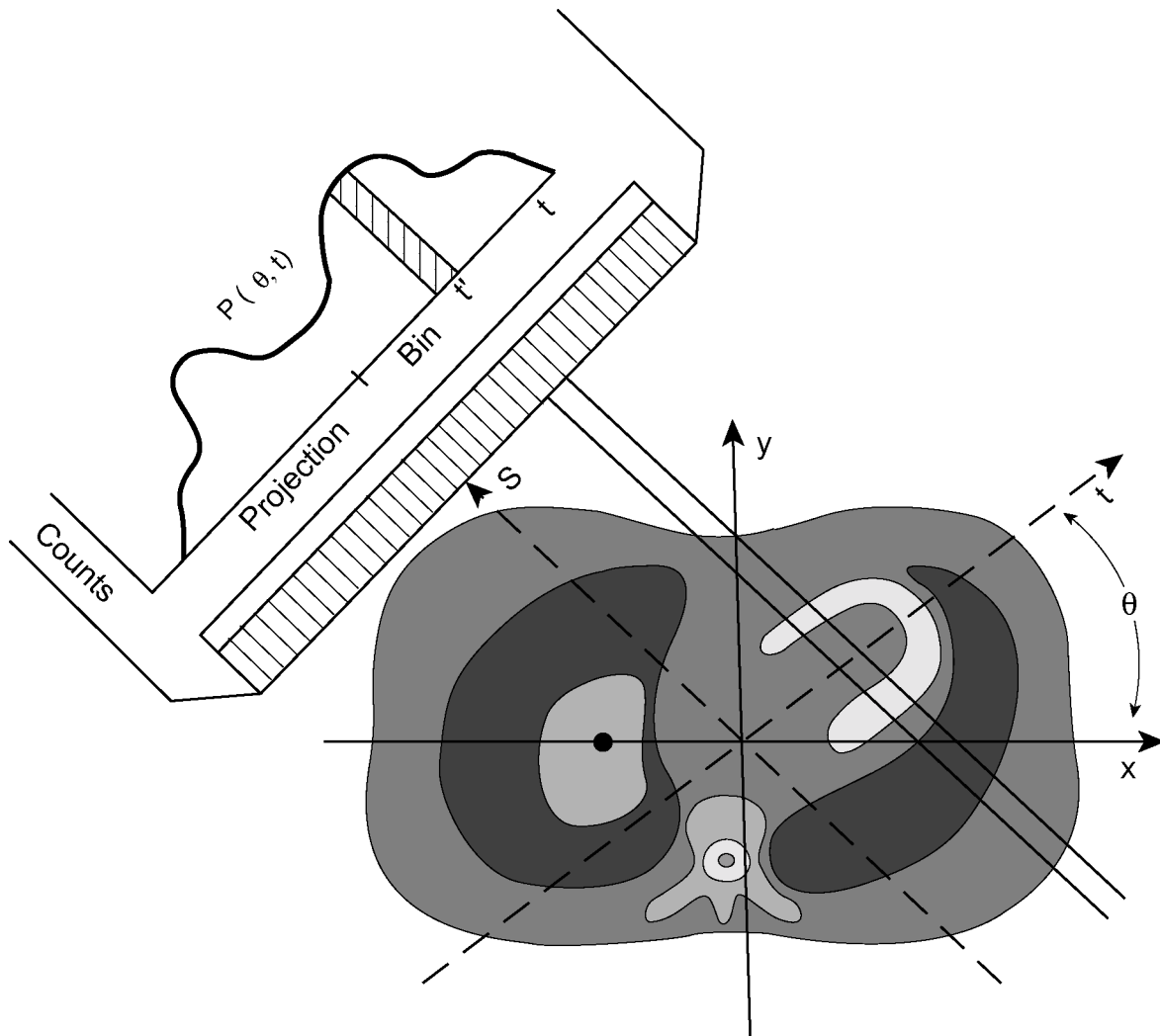
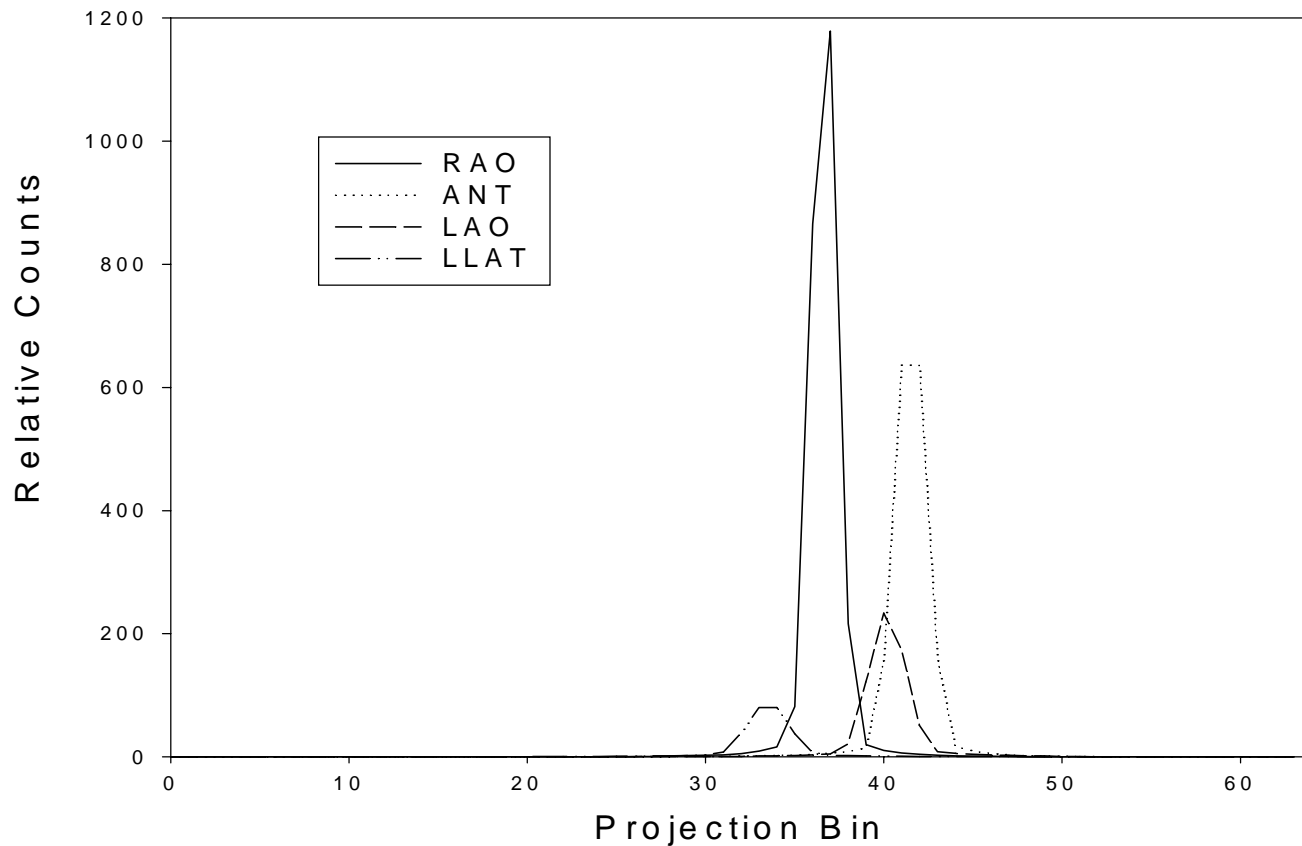Figure 1. Illustration of geometry of ideal SPECT imaging.
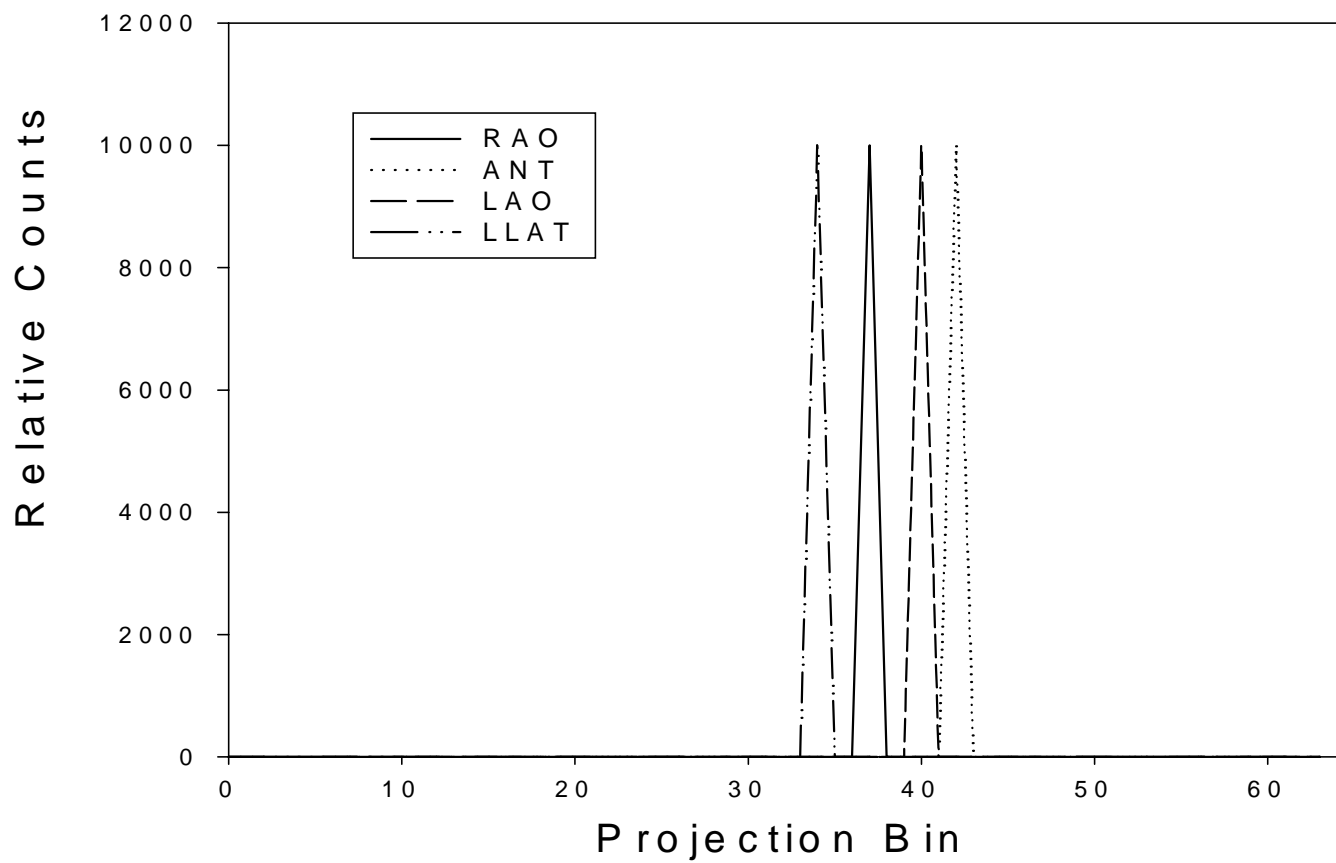
Figure 2. Right anterior oblique (RAO), anterior (ANT), left anterior oblique (LAO), and left lateral (LLAT) projections of a point source in the liver of the MCAT phantom as imaged with no sources of degradation. Note the consistency in size and shape of the projections.
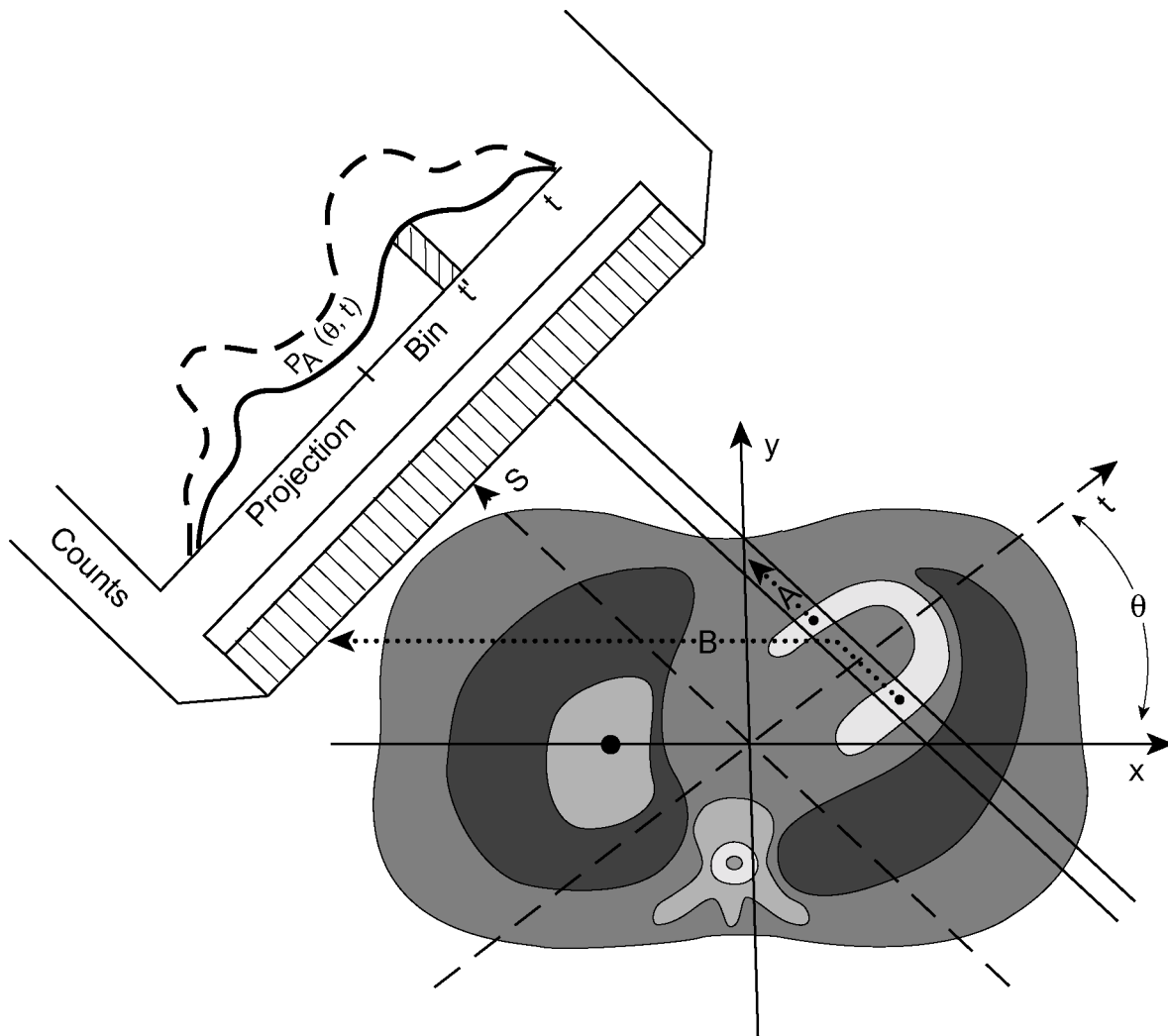
Figure 3. Illustration of impact of attenuation on SPECT imaging. Note that photon A is stopped photoelectrically, and photon B is scattered such that it is not detected. The result is a decrease in the counts in the projection data as illustrated.
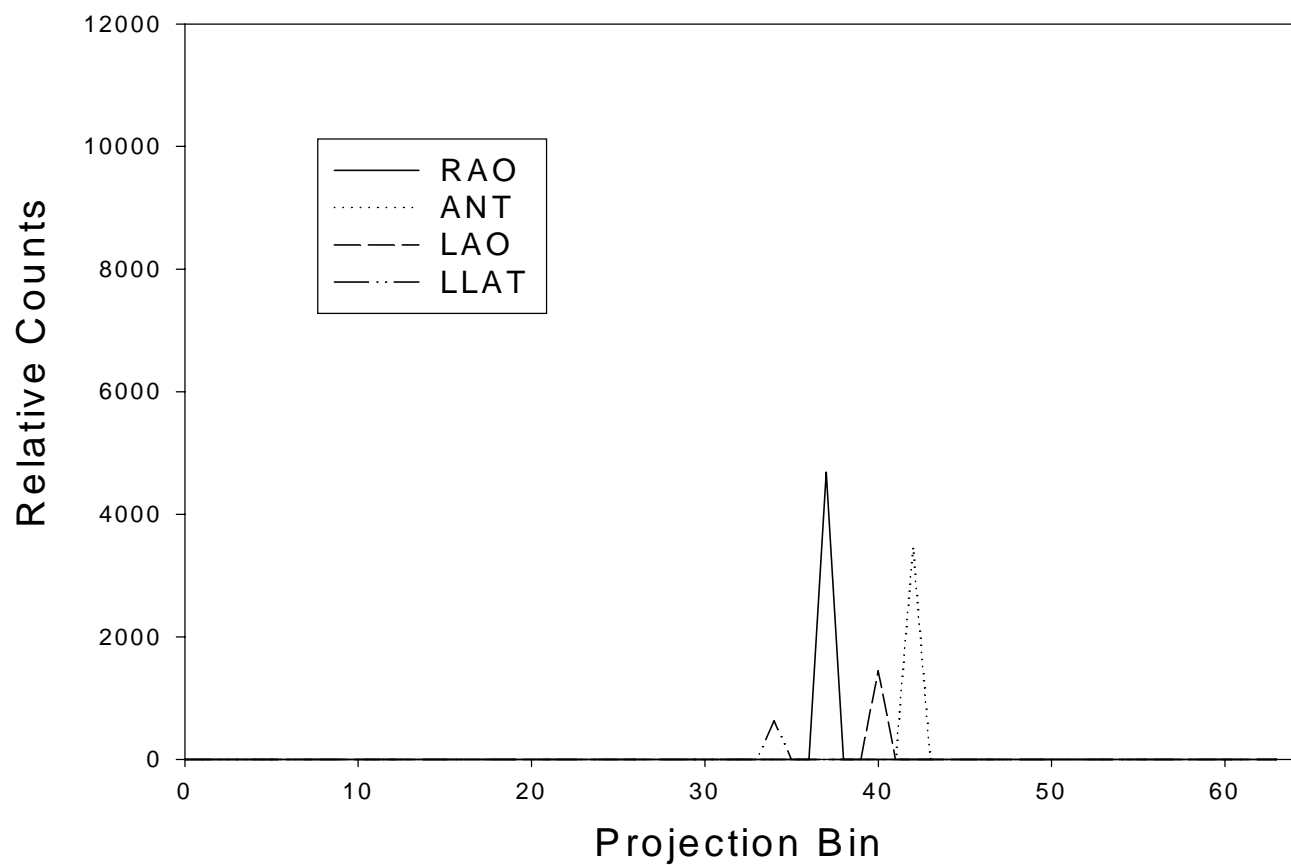
 Figure 4. Right anterior oblique (RAO), anterior (ANT), left anterior oblique (LAO), and left lateral (LLAT) projections of a point source in the liver of the MCAT phantom as imaged with attenuation of the photons. Note the lack of consistency in size and shape of the projections, and their decrease compared Figure 2.
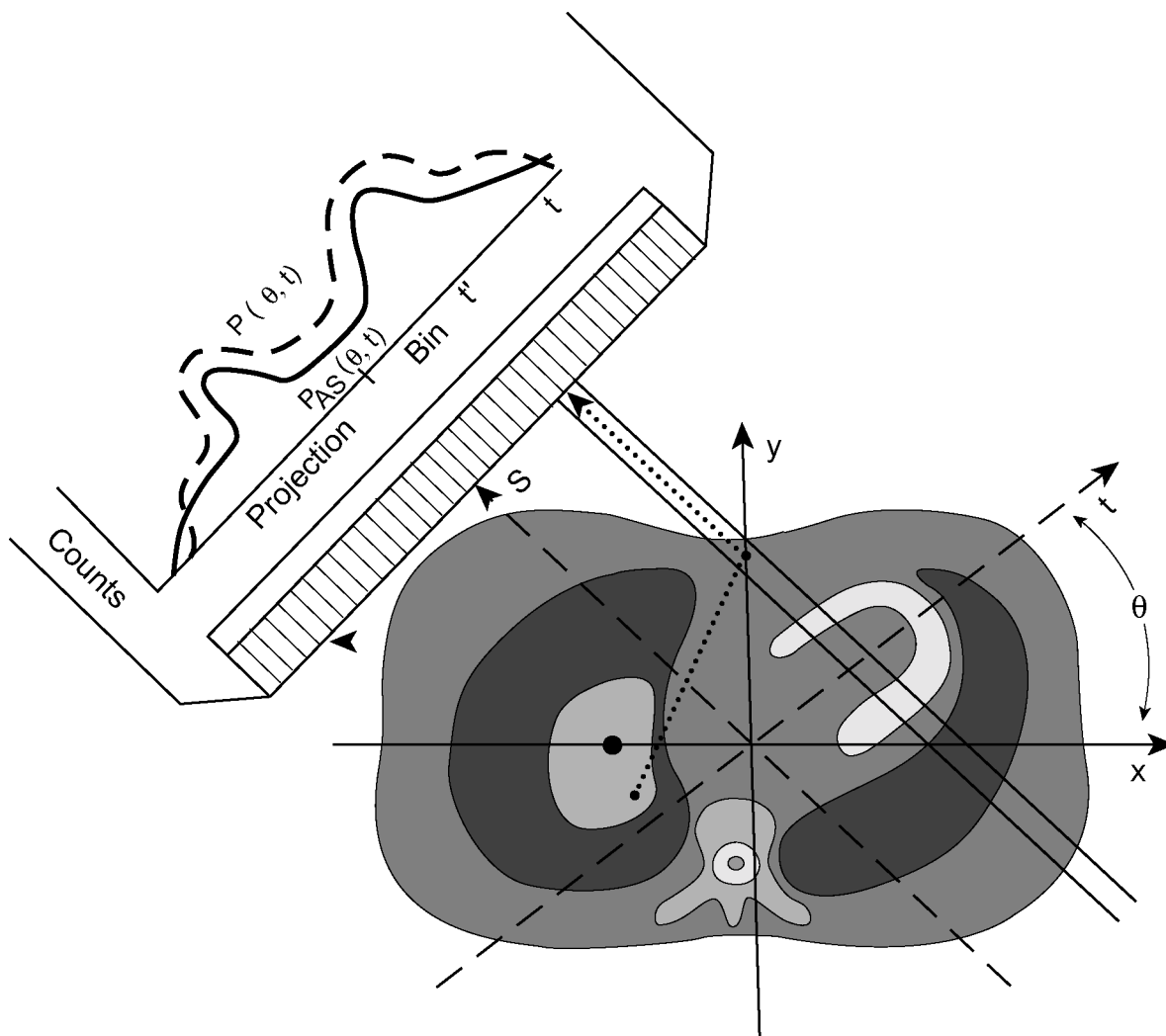
Figure 5. Illustration of impact of scatter on SPECT imaging. Notice the addition of the photon from the liver scattered such that it appears at the incorrect location within the projections.
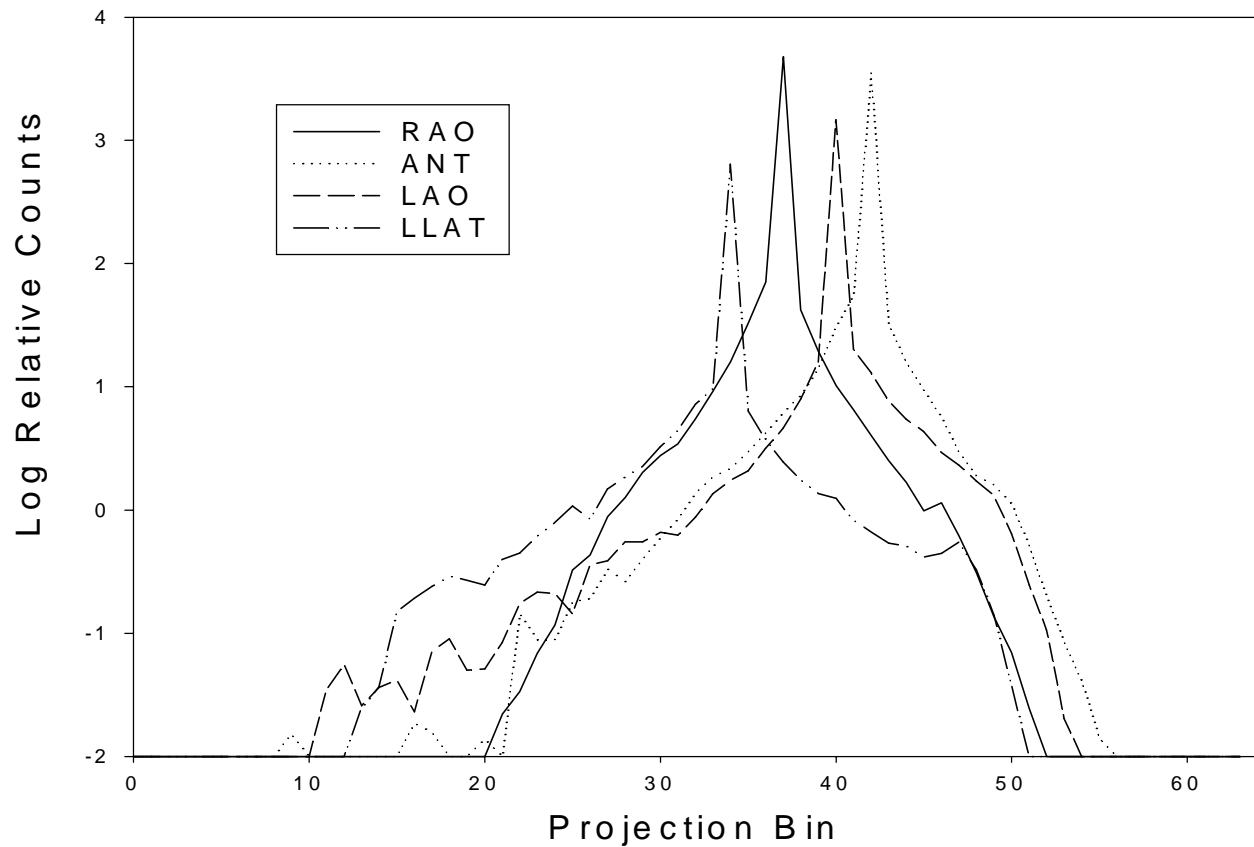
Figure 6. Right anterior oblique (RAO), anterior (ANT), left anterior oblique (LAO), and left lateral (LLAT) projections of a point source in the liver of the MCAT phantom as imaged with attenuation and scattering of the photons. Note the extended tails of the PSF's and the use of logarithmic scaling to make these tails better visible.
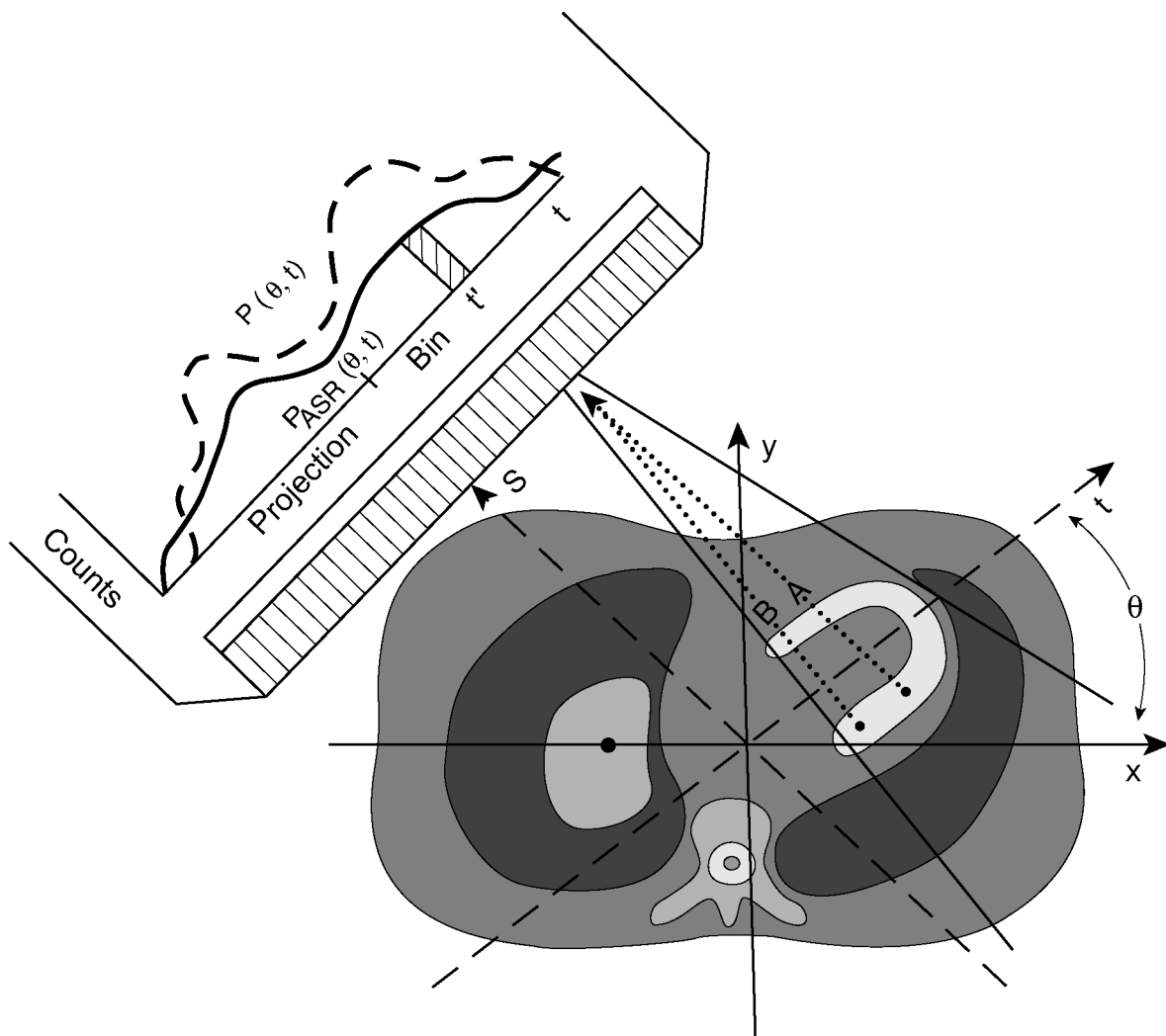
Figure 7. Illustration of impact of system spatial resolution on SPECT imaging. Notice the distance-dependent enlargement of the region from which primary photons can contribute to the projections without penetrating the collimator.

Figure 8. Right anterior oblique (RAO), anterior (ANT), left anterior oblique (LAO), and left lateral (LLAT) projections of a point source in the liver of the MCAT phantom as imaged with attenuation and scattering of the photons, and nonstationary spatial resolution of the system. Note the variation in width and the use of different scaling compared to Figures 2 and 4. Note also that the low magnitude of the scatter tails with linear mapping of the relative counts.
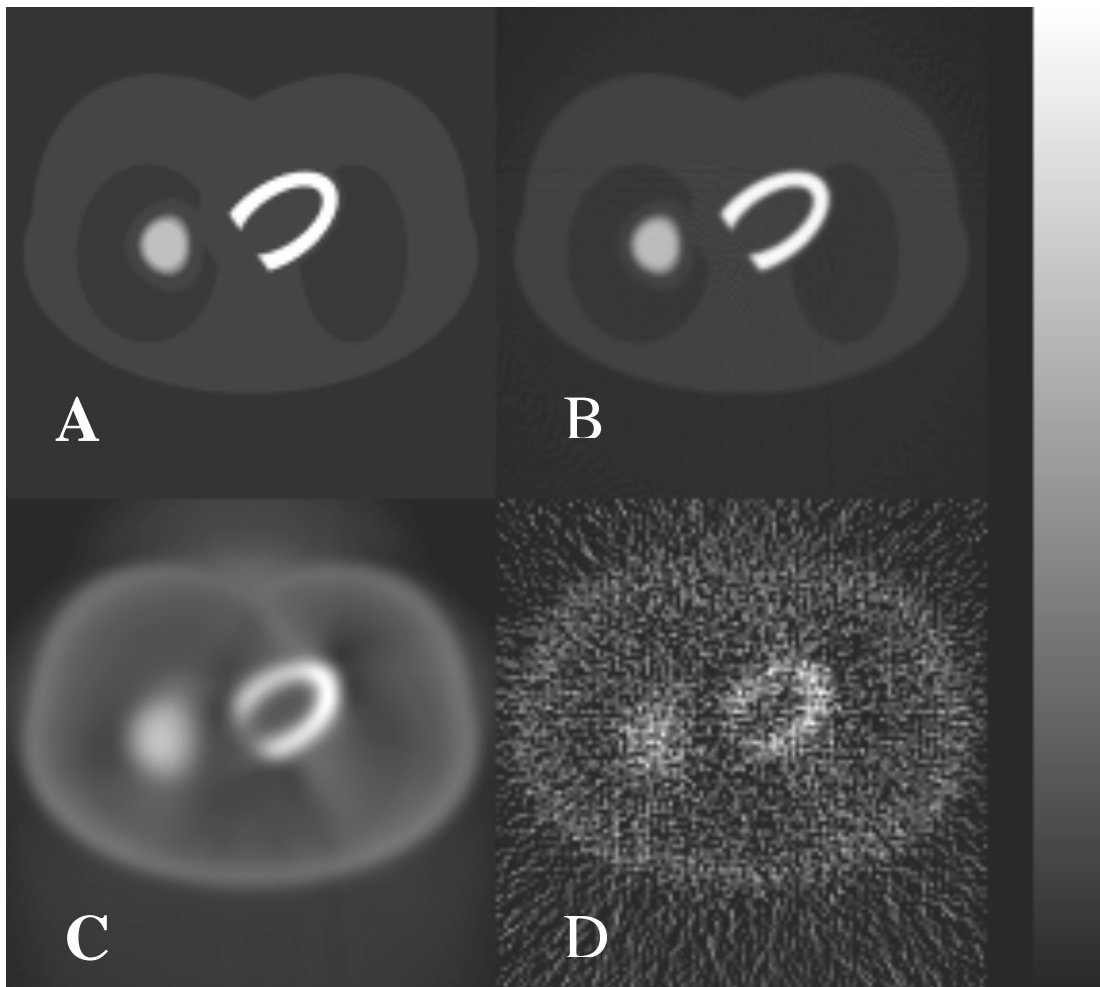
Figure 9. A. Original source distribution from the MCAT phantom. B. FBP reconstruction of ideal projections of source distribution. C. FBP reconstructions of projections degraded by the presence of attenuation, scatter, and system resolution. D. FBP reconstructions of projections degraded by the presence of attenuation, scatter, system resolution, and noise.
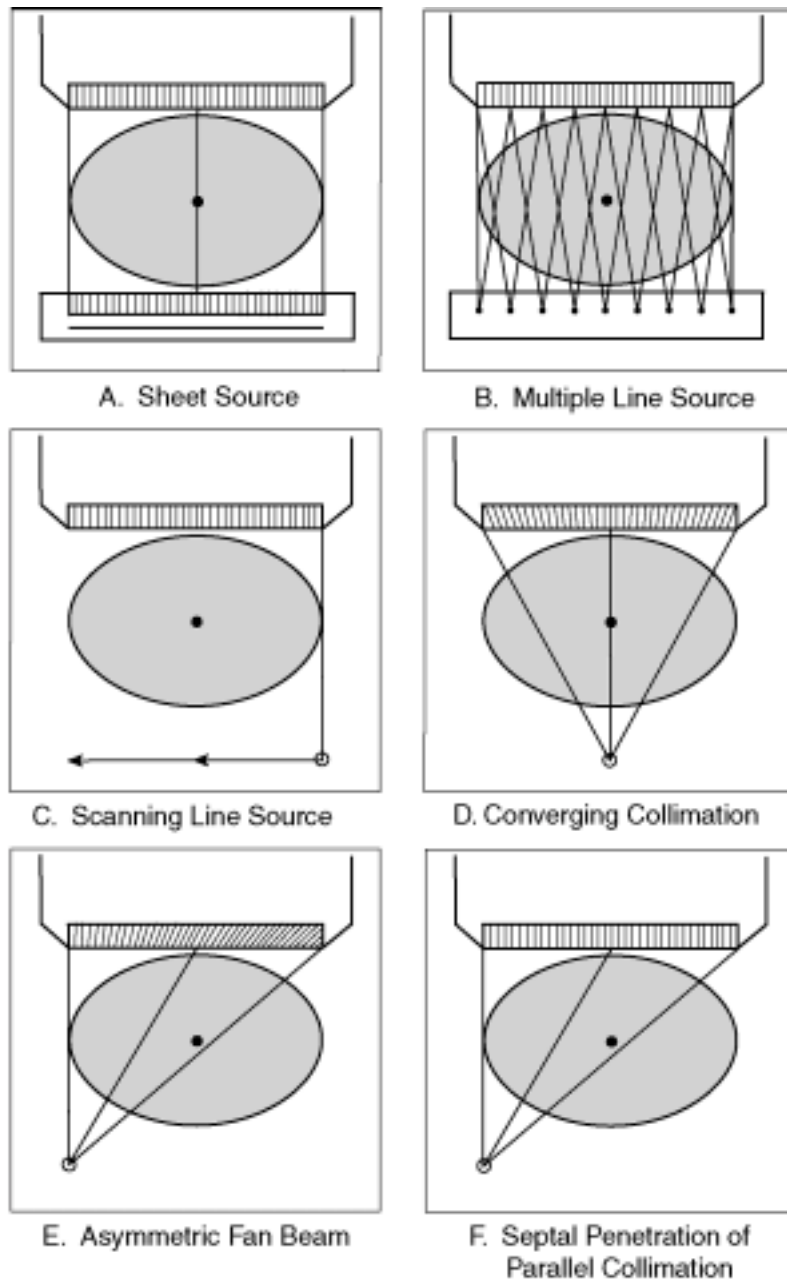
Figure 10. Different configurations for transmission imaging on a SPECT system.
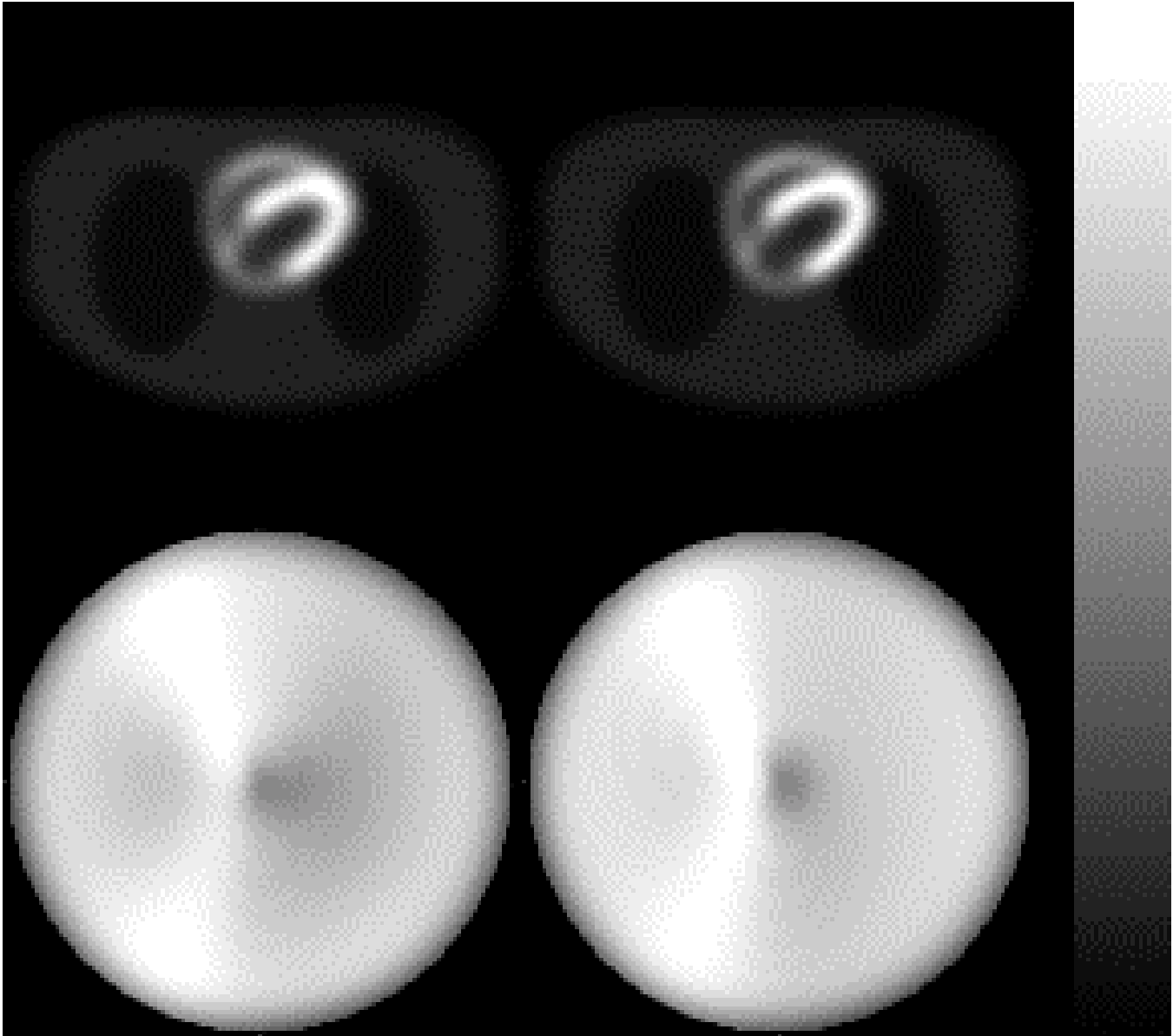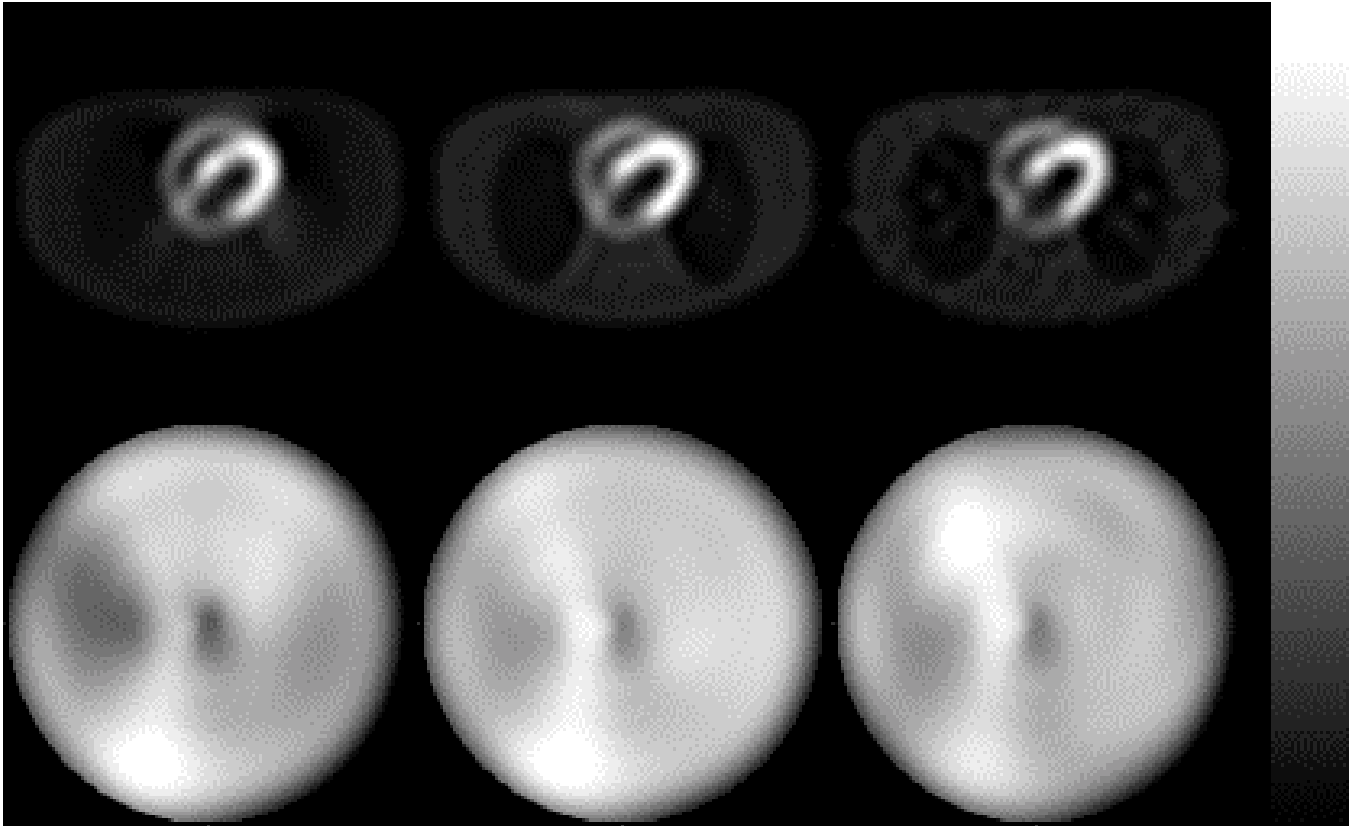
Figure 11. Comparison of FBP reconstructions without attenuation correction of MCAT phantom simulations which included solely the influence of distance-dependent resolution. Top row shows reconstructions of transverse slice illustrated in Figure 1. Bottom row shows polar maps. Left column is for 180^0 reconstruction, and right row is for 360^0 reconstruction. Reproduced with permission from [53].
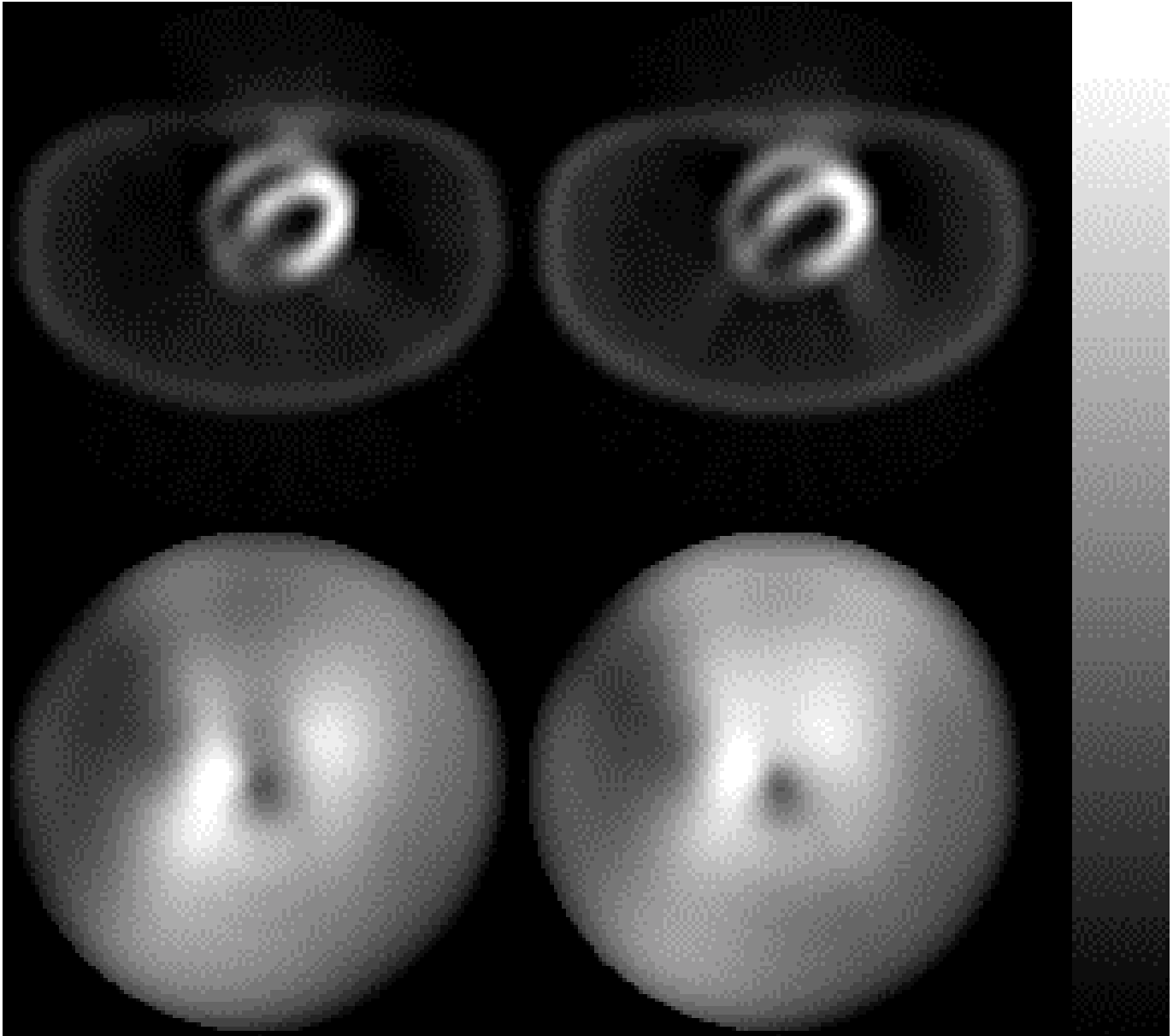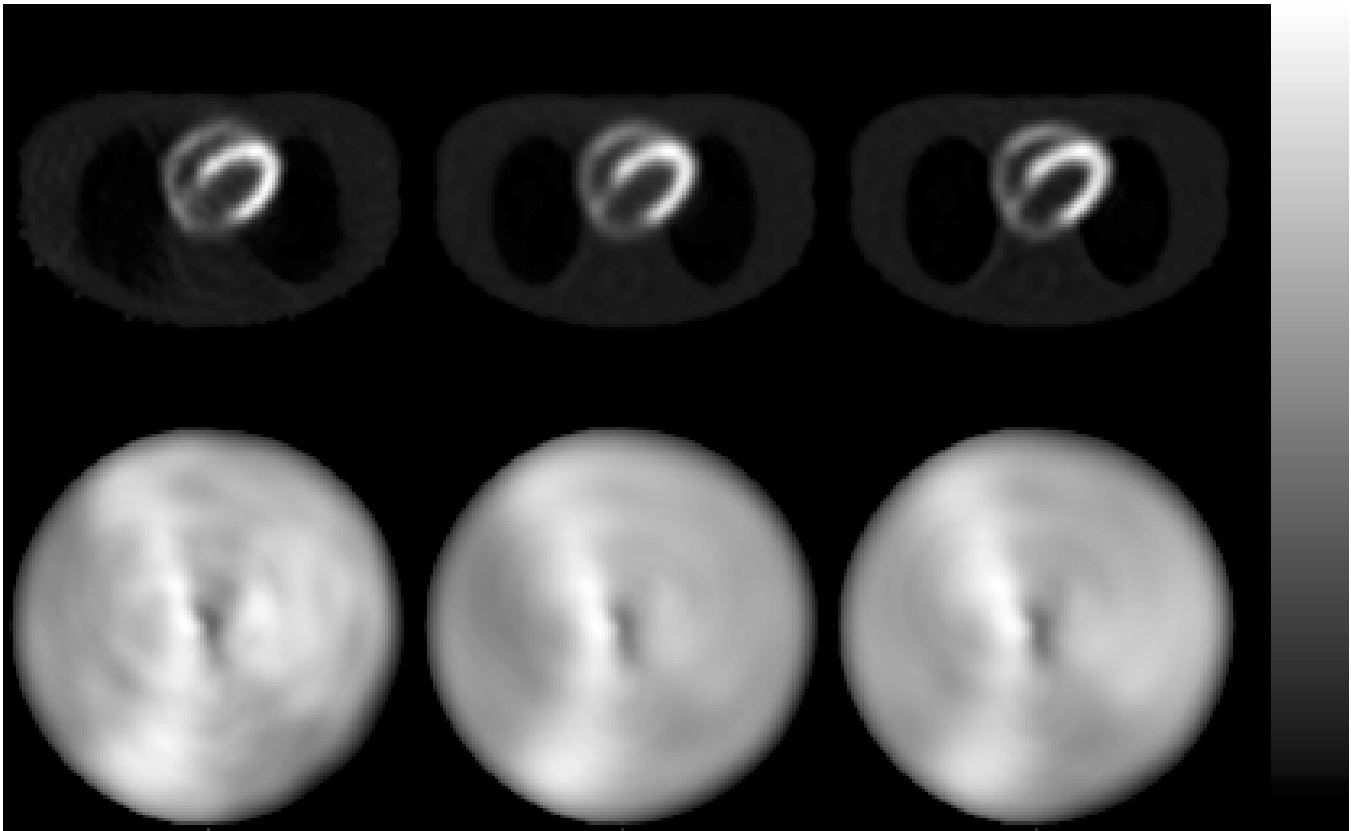
Figure 12. Comparison of FBP reconstructions without attenuation correction of MCAT phantom simulations that included influence of distance-dependent resolution and attenuation. Top row shows reconstructions of transverse slice through LV. Bottom row shows polar maps. Left column is for 180^0 reconstruction, and right row is for 360^0 reconstruction. Reproduced with permission from [53].

Figure 13. Comparison of FBP reconstructions with Chang attenuation correction of MCAT phantom simulations which included influence of distance-dependent resolution and attenuation. Top row shows reconstructions of transverse slice through LV. Bottom row shows polar maps. Left column is for zeroth order or multiplicative Chang. Middle column is for one iteration of Chang. Right column is for five iterations of Chang. Reproduced with permission from [53].

Figure 14. Comparison of MLEM reconstructions with attenuation correction of MCAT phantom simulations which included influence of distance-dependent resolution and attenuation. Top row shows reconstructions of transverse slice through LV. Bottom row shows polar maps. Left column is 30 iterations of 180^0 reconstruction. Middle column is for 30 iterations of 360^0 reconstruction. Right column is for 100 iterations of 360^0 reconstruction. Reproduced with permission from [53].
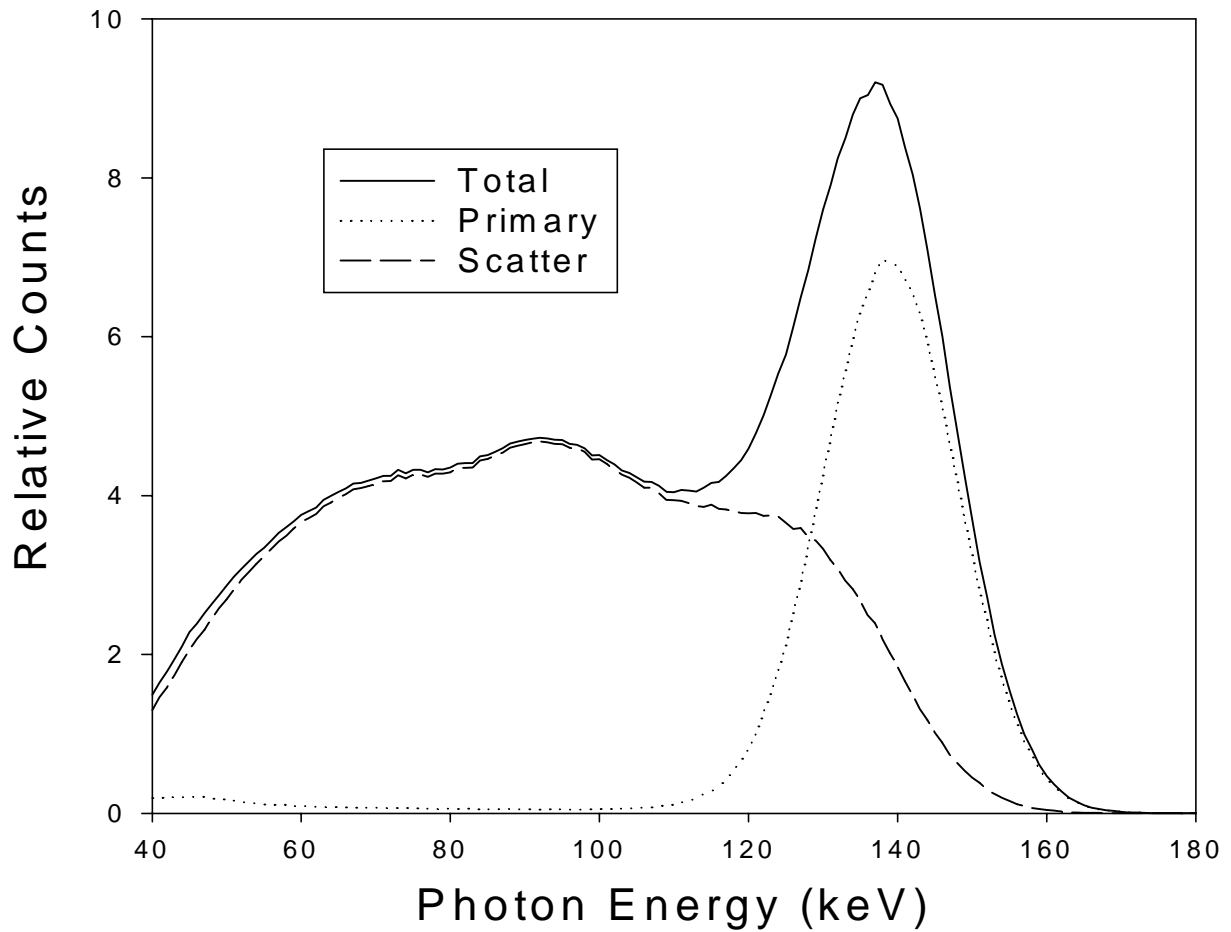
Figure 15. Total, primary, and scatter energy spectrums generated using the SIMIND Monte Carlo package for an LAO view of a simulated Tc-99m sestamibi distribution in MCAT phantom.
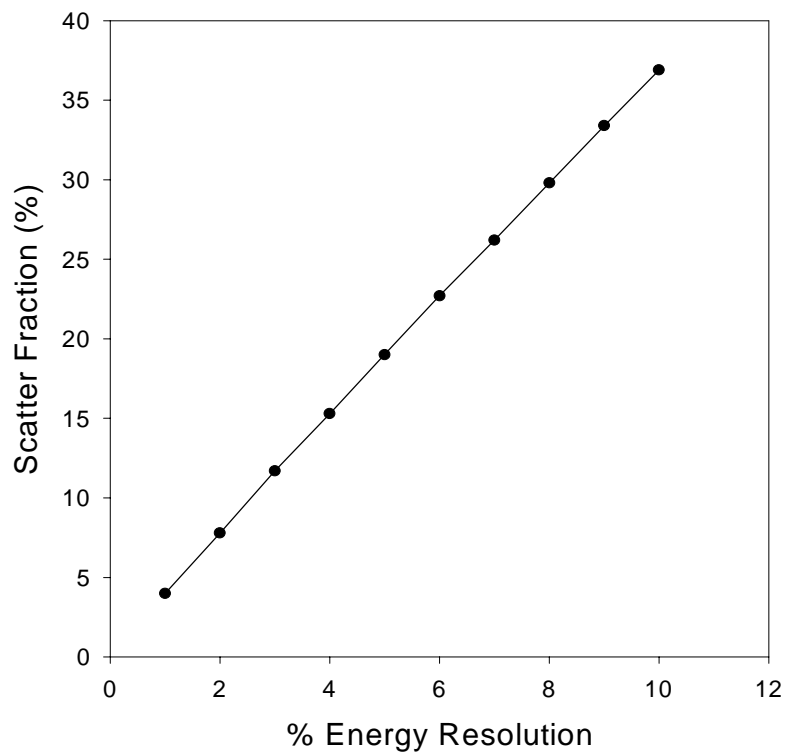
Figure 16. Plot of % scatter fraction versus % energy resolution of imaging system for LAO view of SIMIND simulated Tc-99m sestamibi distribution in MCAT phantom.
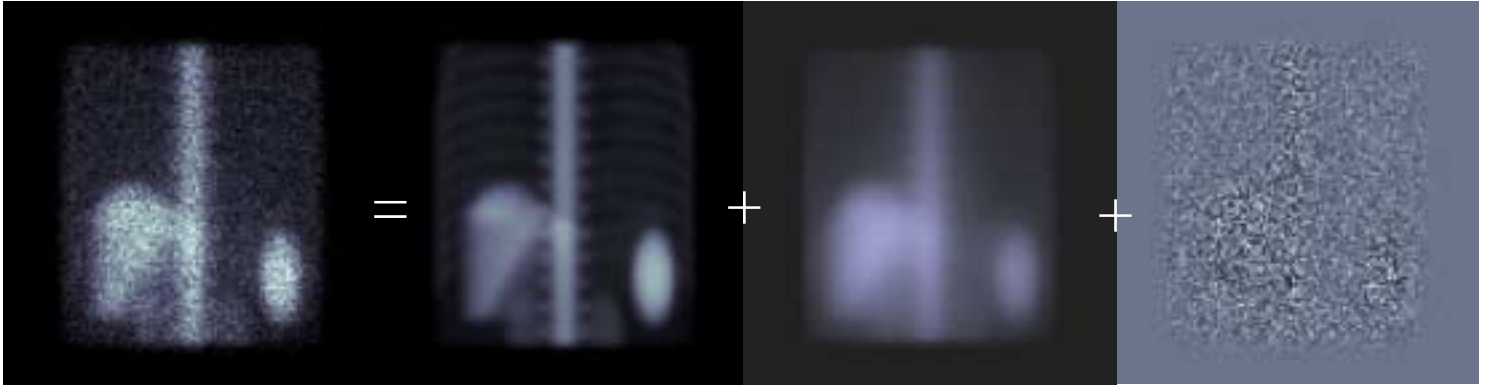
Figure 17. Monte Carlo simulated posterior views of a Ga-67 distribution within the MCAT phantom illustrating the problem with scatter estimation. From left to right are shown the noisy projection, a "noise-free" primary only projection, a "noise-free" scatter only projection, and the noise added to the middle two projections to produce the projection on the far left. Note each image is independently scaled, and the noise image on the far right contains both positives and negatives with the medium shade of gray around the outside representing zero.
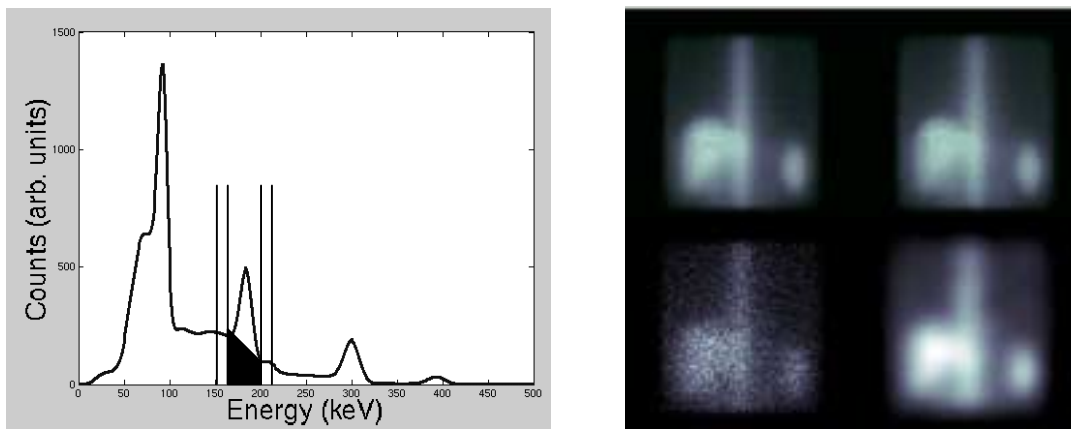

Figure 18. On the left is shown a Ga-67 energy spectrum with TEW windows and scatter estimate indicated for its 185 keV photon. On the right side is shown the actual Monte Carlo simulated scatter distribution in a posterior projection of a Ga-67 source distribution, the TEW estimate from "noise free" projections, the TEW estimate for noisy projections, and the low-pass filtered TEW estimate from the noisy projection data.
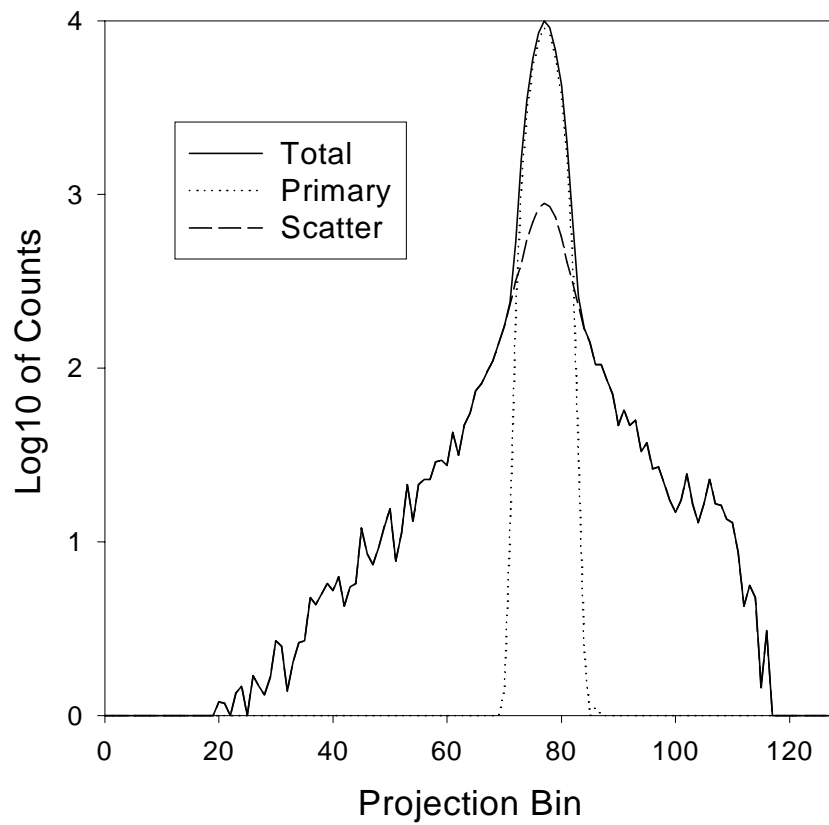
Figure 19. Plot of SIMIND simulated total, primary and scatter PSF's for LAO view of a slice centered on axial location of a Tc-99m point source located in the left ventricular wall of the MCAT phantom. Note asymmetry of the scatter response.

Last ┌──────────────────┐ +Max

Projection
Angle   Sinogram   2D FFT →   Far   Near   Angular
                                                   Near   Far   Frequency (w)   0

First └──────────────────┘ -Max
      First   Last   -Max   0   +Max
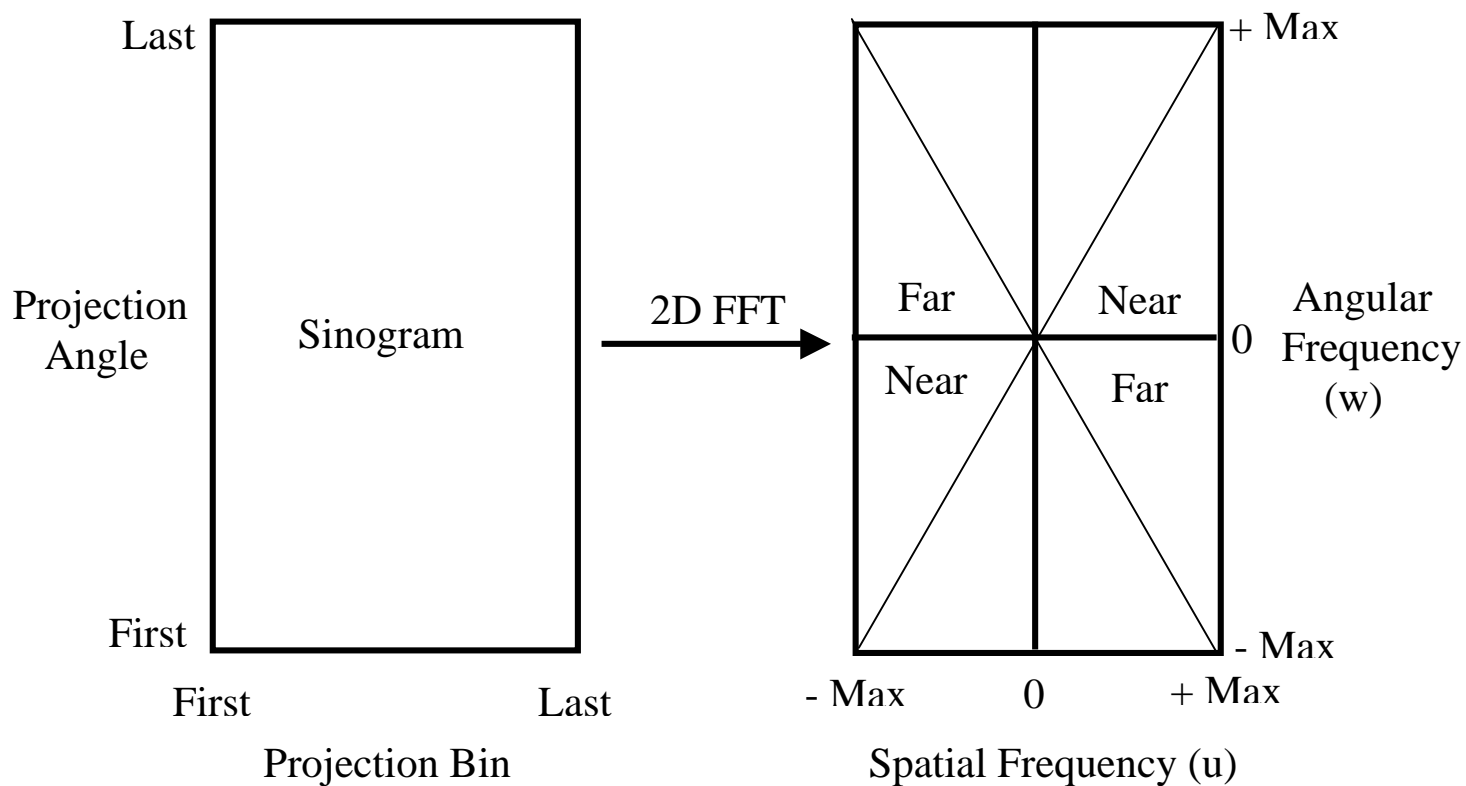   Projection Bin   Spatial Frequency (u)

Figure 20. Drawing illustrating the frequency-distance relationship between sinogram and its two-dimensional fast-Fourier transform.
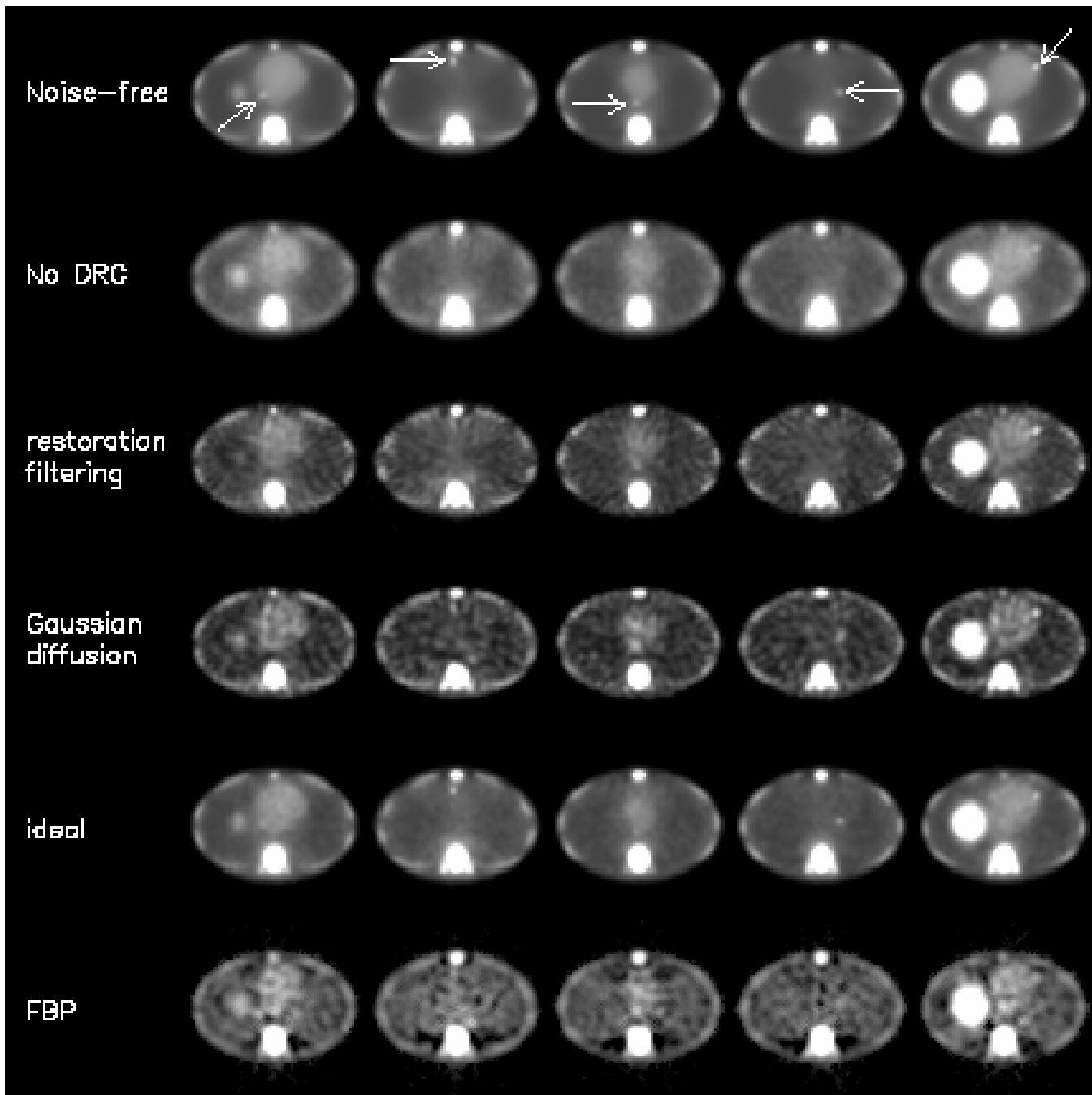
Figure 21. Examples of observer study images. Along top row arrows in the noise-free images reconstructed with the "ideal" DRC strategy indicate tumor locations. Noise realizations of the same slices are shown beneath for each of the DRC strategies. Reproduced with permission from [130].